学位論文（要約）

Interannual variability of the western boundary currents in the southern Indian Ocean
(南インド洋における西岸境界流の経年変動)

平成 29 年 12 月博士（理学）申請

東京大学大学院理学系研究科

地球惑星科学専攻

山上　遥航

Abstract

The Agulhas Current is a strong western boundary current transporting heat and water poleward along the southern Africa, and influences not only the local climate and biodiversity but also the global thermohaline circulation. Since the solitary meander of the Agulhas Current, called the Natal Pulse, explains the large part of the variance of the Agulhas Current, and triggers the early retroflection of the Agulhas Current and thus the pinch-off of the Agulhas Ring in the Agulhas Retroflection region, the Natal Pulse is a key phenomenon in this region. To understand interannual variability of the Agulhas Current, this thesis is devoted to clarify the mechanism of interannual variations in the Natal Pulse and that in the source regions of the Natal Pulse, i.e. the Northeast/Southeast Madagascar Currents (NEMC/SEMC).

From an analysis of an observational data (AVISO) and high-resolution model (OFES) outputs, it is found that most of the Natal Pulse is triggered by anticyclonic eddies propagating from the upstream regions. An eddy kinetic energy (EKE) budget analysis shows that the barotropic conversion due to the mean horizontal shear of the Agulhas Current and the advection of EKE dominate the tendency of EKE during the growth of the Natal Pulse. Hence, the interaction between the mean horizontal shear and anticyclonic eddies plays a crucial role in the generation of the Natal Pulse. An automated eddy-tracking method also reveals that sources of these anticyclonic eddies originate from mainly the SEMC.

Since the Natal Pulse shows interannual variations in the AVISO and OFES, the mechanism of interannual variations is also examined for the first time. Using a simple statis-

tical model, it is found that anticyclonic eddies from the SEMC region is relatively important. An energy conversion analysis off the southern coast of Madagascar shows that the barotropic conversion is the main energy source and corresponds to the interannual variations of anticyclonic eddies in this region. Therefore, interannual variations of the SEMC plays a critical role in the interannual variations of the Natal Pulse. Also, no bottom trapped eddy is found during the generation of the Natal Pulse, and the amplitude of the anticyclonic eddy is one of the necessary conditions for the generation.

Since the importance of the interannual variations in the SEMC is shown, the dynamics of interannual variability of the NEMC and SEMC has been examined. From the analysis of observational and reanalysis data, it is found that interannual variations of the NEMC/SEMC transports are due to those of the South Equatorial Current (SEC) rather than SEC bifurcation latitude (SBL). The Time-dependent Island Rule (TDIR) reproduces the interannual variations and reveals the major role of the meridional transport anomaly in the interior region in the interannual variations of the SBL, NEMC, and SEMC. The variance of the meridional transport is mainly explained by geostrophic transport anomalies in $60°$-$90°$E and thus wind stress curl anomalies.

Since wind stress curl anomalies in the interior are affected by climate modes, the relationship between the SBL, NEMC, SEMC, and climate modes are examined. Interannual variations of the SBL, and the NEMC/SEMC are correlated with the Niño 3.4 with a lag of 5-15 months. Reanalysis data shows that wind stress curl anomalies in the central Indian Ocean is a response to the diabatic heating anomalies in the western Pacific Ocean associated with the ENSO, and partly modified by the local SST forcing in the southeastern Indian Ocean. AGCM sensitivity experiments support the results from the reanalysis data and further shows that the Pacific SST is the major forcing mechanism of the wind stress anomalies while the southeastern Indian SST can generate up to 50% of the wind stress curl anomalies.

Contents

Chapter 1

General introduction

1.1 The Agulhas Current

The Agulhas Current[1] is one of the strongest western boundary currents in the world oceans, transporting tremendous amount of water mass and heat poleward along the South African coast (Fig. 1.1). Its water mainly originates from mesoscale eddies from the Mozambique Channel, and Northeast and Southeast Madagascar Currents (NEMC and SEMC). Further upstream, almost half of the water in the NEMC and SEMC are fed by water mass from the South Equatorial Current (SEC), while the other comes from the south of Australia as a branch of the subtropical gyre in the intermediate layer (Durgadoo et al. 2017). Because of its unique characteristics, the Agulhas Current attracted many oceanographers in recent decades (Lutjeharms 2006).

The mean poleward volume transport obtained from in-situ observations ranges from 69.7 $\pm$ 21.5 Sv (1 Sv=$10^6 m^3 s^{-1}$) (Bryden et al. 2005) to 84 $\pm$ 24 Sv (Beal and Elipot 2016) with its maximum occurring at around 60 km from the coast. The Agulhas Current transport proxies based on regressions between the sea surface height and transport revealed a prominent annual cycle, with the maximum during austral summer (Beal et al. 2015; Beal and Elipot 2016).

Variability of the Agulhas Current is characterized by its meander, so called the "Natal Pulse" (Lutjeharms and Roberts 1988), rather than transport anomalies. The strong horizontal temperature gradient associated with the current and relevant mesoscale eddies has been good targets of infra-red satellite observations; the large deflection of the Agulhas Current was first detected by satellite infra-red images of sea surface temperature (SST) (Harris et al. 1978), and later verified by hydrographic data off the east coast of southern African (Grndlingh 1979). This meander received much attention not only because of its kinematics but also because it may lead to the early retroflection of the Agulhas Current

[1] "Agulhas "is a Portuguese word meaning needles which probably stems from the observation in the 16th century that the needles of compasses showed no magnetic declination at the Golfo das Agulhas (the east of the cape currently called Cape Agulhas) (Lutjeharms 2006). In the Age of Discovery, the Agulhas Current was a big barrier as well as scurvy for Europeans to explore India because of its strong southwestward transport against the direction of adventure.

and thus pinch-off of the Agulhas Ring (van Leeuwen et al. 2000).

1.2 Impact of the Agulhas Current on the regional climate and biodiversity

The strong poleward transport of the Agulhas Current has large impacts on the regional climate and biodiversity around southern Africa. Jury et al. (1993) reported that a statistically significant relationship exists between summer rainfall along the southeastern coast of South Africa and the Agulhas Current, and they suggested that mesoscale structures of the Agulhas Current interact with local weather system and modify alongshore rainfall changes. Although Reason (2001a), Reason et al. (1998), and Reason and Godfred-Spenning (1998) focused mainly on SST anomalies associated with the subtropical Indian Ocean dipole (Behera and Yamagata 2001), anomalous SST in the southwestern Indian Ocean including that related to the Agulhas Current drives climate variability in the southern Africa. Also, air-sea interaction in the Agulhas Retroflection region influences the intensity of the storm-track activity (Reason 2001b), extreme weather events in South Africa (Rouault et al. 2002), and surface wind intensification over a mesoscale eddy (Rouault and Lutjeharms 2000).

Furthermore, dynamical impacts of the Agulhas Current on the coastal regions produce interesting characteristics in the local biodiversity. Strong surface currents in the Agulhas Current determine the distribution of marine animals such as Leatherback sea turtles (Hughes et al. 1998) and Jackass penguins (Randall et al. 1981). Also, upwelling induced by topography in the vicinity of the Agulhas Current (Gill and Schumann 1979) and wind forcing (Leber et al. 2016) feeds the ecosystem in the coastal region (Guastella and Roberts 2016).

1.3 Can the Agulhas Current couple the subtropical gyre in the southern Indian Ocean with the Agulhas Leakage?

Understanding the role of the Agulhas Current in the inter-ocean water mass exchange between the Indian and Atlantic Oceans is a great motivation for in-situ and satellite altimeter observations as well as eddy-resolving numerical simulation. This is because the southwestern Indian Ocean is one of the most eddy-rich oceans owing to the presence of Madagascar (Penven et al. 2006), and mesoscale variability in the Agulhas Retroflection region seems to play a critical role in the global thermohaline circulation (Beal et al. 2011). This water mass exchange is known as the Agulhas Leakage, and influences the stratification of the upper branch of the Atlantic meridional overturning circulation and thus long-term climate variations of the North Atlantic (Biastoch et al. 2008). Biastoch et al. (2015) reported that the Agulhas Leakage and Atlantic Multi-decadal Oscillation (AMO) covary with the Agulhas Leakage with the former leading by 15 years. Since the AMO has profound impacts on the Northern Hemisphere climate (Ting et al. 2009), the exports of warm water to the Atlantic Ocean may modulate the AMO and thus the Northern Hemisphere climate. Biastoch et al. (2009) attributed the recent increase in the Agulhas Leakage to the poleward shift of the westerly wind in the Southern Hemisphere associated with global warming. More recently, Durgadoo et al. (2013) and Loveday et al. (2014) conducted sensitivity experiments that highlight the relative contribution of changes in the westerly and trade winds to decadal variability of the Agulhas Leakage. They concluded that the Agulhas Leakage predominantly responds to strengthening of the westerly wind linearly and the Agulhas Leakage is decoupled from the trade winds.

On the other hand, “upstream control hypothesis” is also a foundation of researches about the Agulhas Current and Leakage (Schouten et al. 2002). In their hypothesis, the Natal Pulse which is triggered by mesoscale eddies from the Mozambique Channel or the south of Madagascar leads to early retroflection of the Agulhas Current and thus the ring shedding. In fact, several studies showed the connection of the Agulhas Current

and the Agulhas Leakage in terms of the Natal Pulse, high-frequency transport anomaly, turbulent choking mechanism, and the retroflection longitude (Arruda et al. 2014; Le Bars et al. 2012; Biastoch and Krauss 1999; Pichevin et al. 1999; van Sebille et al. 2009a, b). Recently, Backeberg et al. (2012) showed the increasing trend of eddy kinetic energy in the Agulhas Retroflection region, Mozambique Channel, and the south of Madagascar. Their result implies the possible spin-up of turbulent motions in the southern Indian Ocean by the trade winds in the recent decades.

As metioned above, some studies suggested decoupling of the Agulhas Leakage from the Agulhas Current on the decadal time scale, while others showed that the Agulhas Current affects the Agulhas Leakage in individual events or on interannual timescale. Thus, the dynamical relationship between the Agulhas Leakage and the Agulhas Current as a part of subtropical gyre in the southern Indian Ocean is still controversial. Therefore, the Agulhas Leakage need to be investigated more in terms of the relation with the Agulhas Current, but the detailed processes about the nonlinear phenomena and their variability in the Agulhas Current have not received much attention.

1.4 Goal of this thesis

To enhance our understanding of the ocean circulation, climate variability, and biodiversity in the southwestern Indian Ocean, and global thermohaline circulation, dynamics and variability of the Agulhas Current, mesoscale eddies, and circulation around Madagascar need to be better understood. Although some studies discussed mesoscale eddies and meanders that originated from the coast of Madagascar, they are mainly based on statistical analyses of observed or simulated sea surface height (Palastanga et al. 2006; Ridderinkhof et al. 2013; Putrasahan et al. 2016), and no study to date showed the dynamical mechanisms behind these apparent connections. Therefore, the key scientific questions to be addressed in this thesis are:

(i) What are the generation mechanism and sources of the Natal Pulse?

(ii) What is the mechanism of interannual variations in the Natal Pulse?

(iii) What is the role of mesoscale eddies on the Natal Pulse?

(iv) What is the dynamical relationship between mesoscale activity and basin-scale wind field?

This thesis is devoted to answering these questions with a special focus on the dynamical mechanisms related to interannual variability of mesoscale activity in the southwestern Indian Ocean. In the next chapter, the generation and interannual variations of the Natal Pulse are examined. In chapter 3, mechanisms of interannual variability of western boundary currents along the Madagascar coast and its relationship with large-scale climate modes are investigated. General conclusion and possible future directions are given in the final chapter.

Figures

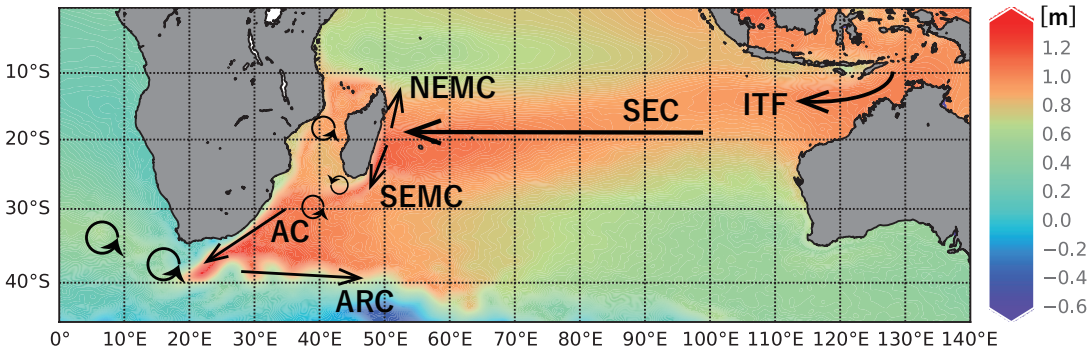

Figure 1.1: Mean dynamical topography (color) from CNES-CLS13 MDT (Rio et al. 2014) and schematically drawn surface currents: Indonesian Throughflow (ITF), South Equatorial Current (SEC), Northeast and Southeast Madagascar Currents (NEMC and SEMC, respectively), Agulhas Current (AC), and Agulhas Return Current (ARC). Circles represent anticyclonic eddies in Mozambique Channel, cyclonic and anticyclonic eddies in the south of Madagascar, and the Agulhas Rings in the Atlantic Ocean.

Chapter 2

Dynamics and interannual variability of the Natal Pulse

This chapter will be submitted as:

Yamagami Y., T. Tozuka, B. Qiu, Dynamics and interannual variability of the Natal Pulse, J. Geophys. Res., in prep.

（非公表部分）

Chapter 3

Interannual variability of South Equatorial Current bifurcation and western boundary currents along the Madagascar coast

This chapter has been published as:

Yamagami, Y., and T. Tozuka (2015), Interannual variability of South Equatorial Current bifurcation and western boundary currents along the Madagascar coast, J. Geophys. Res. Oceans, 120, 8551–8570.

3.1 Introduction

Although the role of the SEMC in the variations of the Natal Pulse has been shown in the previous chapter, the variability of the circulation around Madagascar, particularly the NEMC, SEMC and SEC bifurcation latitude (SBL), are not fully understood. In this regard, Palastanga et al. (2006) investigated interannual variability of sea surface height (SSH) fields and eddy activity in the Mozambique Channel and southwest of Madagascar (van der Werf et al. 2010; Backeberg and Reason 2010; Halo et al. 2014) and pointed out that it is related to westward propagating basin-scale anomalies (Masumoto and Meyers 1998). Although they suggested that these SSH anomalies in the 14°S-15°S band are related to the Indian Ocean Dipole (IOD; Saji et al. (1999)), Rao and Behera (2005) revealed through partial correlation analyses that SSH variability in the 10°S-20°S band is more strongly correlated with the El Niño/Southern Oscillation (ENSO) than IOD. More recently, Zhuang et al. (2013) reported that SSH anomalies around Madagascar are predominantly generated by the wind stress curl input around 75°E-90°E at the mean SBL and the eastern boundary effect associated with the ENSO is relatively small. Regarding the SEMC, which is also known to undergo interannual variations (Nauw et al. 2008), Ridderinkhof et al. (2013) showed that the strength of SEMC estimated using satellite altimetry data is positively correlated with Niño 3.4 index with the latter leading by about 500 days. Also, Palastanga et al. (2006) suggested that the NEMC and SEMC transports decrease (increase) after positive (negative) IOD.

However, these past studies were based mostly on statistical analysis such as correlation analysis and did not perform dynamical analysis. In this regard, Chen et al. (2014) was the first to dynamically investigate the seasonal variation of the SBL. They found that the seasonal variation of the SBL cannot be reproduced by a simple linear Rossby wave model (e.g. Meyers 1979), but it can be explained by a time-dependent version of the Island Rule called “Time-dependent Island Rule” (TDIR) (Godfrey 1989; Firing et al. 1999). This is contrasted with seasonal and interannual-to-decadal variability of the North

Equatorial Current bifurcation latitude in the North Pacific (e.g. Qiu and Lukas 1996; Qiu and Chen 2010; Chen and Wu 2011), which can be well reproduced by a simple linear Rossby wave model. Furthermore, they have shown that Madagascar moderately shifts the phase of the seasonal variation in the SBL owing to the local transport driven by wind stress around the island and the meridionally averaged interior transport. However, their focus was on the seasonal variation and they did not investigate interannual variations in the SBL as well as the western boundary currents along the east coast of Madagascar.

Therefore, after describing seasonal-to-interannual variability of the SBL and the NEMC and SEMC transports in observational and reanalysis data, we investigate the dynamical mechanism of their interannual variability using the TDIR and discuss their link with large-scale climate modes.

This chapter is organized as follows. A brief description of the data is given in the next section. In Sect. 3.3, we first describe the observed interannual variation of the SBL, the NEMC and the SEMC. Then, we use a theoretical model to clarify their dynamical mechanisms in Sect. 3.4. In Sect. 3.5, we discuss their relation with climate modes, and results of sensitivity experiments are shown in Sect. 3.6. Effects of eastern boundary forcing, damping, and nonlinearity are discussed in Sect. 3.7 and the final section summarizes the main results of this chapter.

3.2 Observational and reanalysis data

We use the surface geostrophic current velocity data calculated from absolute dynamic topography (ADT), which is defined as the mean dynamic topography (MDT) plus sea level anomaly (SLA). The altimeter products were produced by Ssalto/Duacs and distributed by AVISO, with support from CNES (http://www.aviso.altimetry.fr/duacs/). We use monthly data from January 1993 to December 2013 with a horizontal resolution of $1/4^\circ \times 1/4^\circ$. Hereafter, we refer to this geostrophic current velocity data as "AVISO geostrophy".

Also, we analyze the dataset from the Ocean ReAnalysis System 4 (ORAS4) of the

European Centre for Medium-Range Weather Forecasts (ECMWF) (Balmaseda et al. 2013). The oceanic component of the ORAS4 is the NEMO, which has a horizontal resolution of $1^\circ \times 1^\circ$ in the extratropics and a refined meridional resolution in the Tropics with a minimum value of 0.3° at the equator. The output is converted into $1^\circ \times 1^\circ$ resolution. There are 42 vertical levels with 18 levels in the upper 200 m. Atmospheric forcing fields are from the ERA-40 (Uppala et al. 2005) for January 1980 to December 1988, and the ERA-Interim (Dee et al. 2011) for January 1989 to December 2009. In addition, ocean data assimilation system (NEMOVAR) is used to assimilate temperature, salinity, and SLAs along altimeter track. We only analyze the output from January 1980 to December 2009 because of the scarce observational data in the southern Indian Ocean before the 1980s. To be compatible with the atmospheric forcing used to produce the ORAS4, the surface wind stress, sea level pressure (SLP), convective precipitation data from the ERA-40 and the ERA-Interim are used for the respective periods. The horizontal resolution of ERA-40 and ERA-Interim are T159 and T255, respectively. All data are interpolated into $1^\circ \times 1^\circ$ resolution.

3.3 Seasonal and interannual variations of the SBL, NEMC, and SEMC

First, we examine seasonal and interannual variations in the SBL. The SBL is defined as the latitude at which the meridional velocity averaged over the western boundary layer ($< 3^\circ$ from the coast) is zero. Here, the western boundary layer is defined as the band in which the meridional velocity averaged from the surface to 400 m depth is larger than 0.05 $[m/s]$ (Fig. 3.1). Since the mean meridional velocity is small from 19°S to 17°S because of its proximity to the mean SBL, the western boundary layer are defined from the Madagascar coast to 51°E in this latitude band and the western boundary layer is smoothly connected in 20°S-19°S and 17°S-16°S. Although many previous studies (e.g. Qiu and Lukas 1996; Chen et al. 2014) defined the bifurcation latitude by the latitude at which the meridional velocity averaged from the coast to 2° off-shore is zero, we use

a different definition because the thickness of the western boundary layer in reanalysis datasets depends on horizontal resolution and a viscosity coefficient.

Figure 3.2a shows the SBL time series calculated from the surface meridional velocity of the AVISO geostrophy and the ORAS4. To extract the low-frequency component, we apply a 15-month running mean (hereafter, the low-pass filter) to these time series. Since the ORAS4 assimilates observed sea level anomalies, it is not completely independent of the AVISO geostrophy. Nevertheless, we compare the SBL obtained from the assimilation product and the AVISO geostrophy (Fig. 3.2a). Here, the SBL of the ORAS4 is calculated using the surface meridional velocity and the definition of the western boundary layer is the same as the previous paragraph except that the surface velocity is used here. Due to poleward tilting of the SEC bifurcation with increasing depth (Chen et al. 2014), the SBL at the surface is located to the north of the 400 m-mean SBL.

The climatological SBL in the ORAS4 (AVISO) moves to the southernmost position in July (August) and the northernmost position in November (Fig. 3.2b). This seasonal variation is in agreement with Chen et al. (2014), both in terms of phase and amplitude. The SBL also undergoes interannual variations with the amplitude of about 2 degrees (Fig. 3.2c), which is comparable to that of seasonal variation (Fig. 3.2b). Since the correlation coefficient between two time series of the interannual anomaly in the SBL (Fig. 3.2c) is 0.54, which is significant at the 90% confidence level, the ORAS4 captures the interannual variation of the SBL reasonably well compared with the AVISO.

Then, we have checked how the volume transports of the NEMC and SEMC are related to the SBL and the SEC transport in the ORAS4. Here, the NEMC and SEMC transports are defined as the volume transport from the surface to 400 m depth within the western boundary layer across 14°S and 24°S, respectively, while the SEC transport is defined as that through the meridional section from 14°S to 24°S at 52°E. The SEC transport is almost equal to the sum of the NEMC and SEMC transports (Fig. 3.3). The seasonal variation of the NEMC and SEMC is almost in phase with that of the SEC, and is negatively correlated with the SBL (Fig. 3.4). For the interannual variations, the stan-

dard deviation of the SEMC transport (1.7 Sv) is smaller than the NEMC transport (2.1 Sv). The larger variance of the NEMC is consistent with the observation (Swallow et al. 1988). The NEMC (SEMC) transport is strongly correlated with the SEC transport with the correlation coefficient of 0.95 (0.91), which is significant at the 90% confidence level (Fig. 3.4). On the other hand, the correlation between the SBL and the NEMC (SEMC) transport is weakly negative with -0.28 (-0.52), and both correlation coefficients are not significant at the 90% confidence level. It is interesting to note that this is contrasted with the situation in the North Pacific, where transport variation of Kuroshio does not coincide with that of the North Equatorial Current but with its bifurcation latitude (Qiu and Lukas, 1996).

As reported by previous studies (Backeberg and Reason 2010; Halo et al. 2014b) and shown in Sect. 2.3, the northern and southern edges of Madagascar are the main vorticity source regions. Therefore, it is of interest to calculate the time series of relative vorticity in these two regions (Fig. 3.5), and compare them with the time series of the SBL and the NEMC and SEMC transports (Fig. 3.6). The relative vorticity is calculated from the AVISO geostrophy, because it has fine enough resolution to resolve the velocity shear in the narrow western boundary layer. The interannual anomaly of relative vorticity at the northern and southern edges has weak correlation with the SBL (-0.39 and 0.20, which are not significant at the 90% confidence level, respectively) (Fig. 3.6a). Although the correlation coefficients between the low-passed NEMC (SEMC) transport and the vorticity at the northern (southern) tip of Madagascar (0.65 and -0.70) are not significant at the 90% confidence level, the correlation coefficients of raw time series (0.21 and -0.33) are significant at the 99% confidence level (Figs. 3.6b, c). Thus, the present results not only support the earlier studies (Palastanga et al. 2006; Backeberg and Reason 2010; Halo et al. 2014b), but also suggest that the variability of the vorticity generation at the both edges of Madagascar is related to the transport anomaly of NEMC and SEMC associated with that of the SEC.

3.4 Mechanism

3.4.1 Time-dependent Island Rule

Since low-frequency variations of the SBL, NEMC, and SEMC are expected to be a response to the Sverdrup transport in the interior and the westward propagation of Rossby waves under the constraint of the existence of the Madagascar island, we use the TDIR (Firing et al. 1999) following Chen et al. (2014). The TDIR is an extension of the Island Rule (Godfrey 1989) to the time dependent case in which the dynamical field is dominated by vorticity input from wind stress curl and westward propagation of baroclinic Rossby waves. Using a linearized 1.5-layer reduced gravity model, the transport within the western boundary layer at an arbitrary latitude ($T_{bc}(y,t)$) is expressed as

$$T_{bc}(y,t) = -T_{in}(y,t) + \int_{y}^{y_n}\int_{x_{w+}}^{x_e} \frac{\partial h}{\partial t} dxdy + T_{in}(y_n,t) + T_{bc}(y_n,t), \quad (3.1)$$

or

$$\begin{aligned} T_{bc}(y,t) &= -T_{in}(y,t) + \frac{1}{\Delta y}\int_{y_s}^{y_n} T_{in}(y,t)dy \\ &\quad + \frac{1}{\Delta y}\oint_{C_1} \frac{\boldsymbol{\tau}(t)\cdot d\boldsymbol{I}}{\rho_0 \beta} \\ &\quad + \int_{y}^{y_n}\int_{x_{w+}}^{x_e} \frac{\partial h}{\partial t} dxdy - \frac{1}{\Delta y}\int_{y_s}^{y_n}\int_{x_{w+}}^{x_e} (y-y_s)\frac{\partial h}{\partial t} dxdy. \end{aligned} \quad (3.2)$$

Here, x and y correspond to the zonal and meridional directions, respectively, $\boldsymbol{dI}$ is the unit vector tangential to the integral path, t indicates the time (Fig. 3.7a),

$$h(x,y,t) = \frac{1}{C_R}\int_{x_e}^{x} B(x', y, t - \frac{x-x'}{C_R})dx', \quad (3.3)$$

is the upper layer thickness anomaly, and x' is a point along the characteristic line of the linear Rossby wave ($x - tC_R = const.$).

$$\begin{aligned} T_{in}(y,t) &= \int_{x_{w+}(y)}^{x_e(y)} Hv dx \\ &= \int_{x_e}^{x_{w+}} \frac{\tau^x}{f\rho_0} dx' - \frac{Hg'}{C_R f} \int_{x_e}^{x_{w+}} B(x', y, t - \frac{x - x'}{C_R}) dx' \end{aligned} \tag{3.4}$$

is the meridional transport in the ocean interior, x_e, x_{w+}, y_s, and y_n represent the eastern boundary, the boundary between the western boundary layer and the ocean interior, the latitude of the southern tip of an island, and the latitude of the northern tip of an island, respectively, and C_1 is the path A'A"DC"C'B' (Fig. 3.7a). Also, $\rho_0 (= 1025\ kg\ m^{-3})$ is the reference density of the seawater, f is the Coriolis parameter, β is the meridional gradient of the Coriolis parameter, $g' (= 0.029\ m\ s^{-2})$ is the reduced gravity, τ^x is the zonal wind stress, $\boldsymbol{\tau}$ is the wind stress vector, $\Delta y = y_n - y_s$, $B(x,y,t) = -\nabla \times (\boldsymbol{\tau}/\rho_0 f)$, $H (= 290\ m)$ is the mean upper layer thickness, and $C_R (= -\beta g' H/f^2)$ is the phase speed of the first baroclinic mode Rossby wave.

Equation (3.1) indicates the volume balance in the area enclosed by AA'A"B"B'B (Fig. 3.7a); the meridional transport within the western boundary layer balances with "the interior transport at the same latitude", "the upper layer thickness anomaly" (hereafter we refer to this effect as "Storage"), and "the net transport between the island and the eastern boundary at $y = y_n$" (Fig. 3.7b). $T_{in}(y_n, t) + T_{bc}(y_n, t)$ can be rewritten as Eq. (3.2). The terms on the top, middle, and bottom rows of Eq. (3.2) represent "inflow from the ocean interior", "local transport driven by the wind stress around the island", and "storage in the interior", respectively (Fig. 3.7c).

As shown in Eq. (3.4), the meridional transport in the interior (T_{in}) can be further decomposed into the Ekman and geostrophic transports. The first term on the right hand side of Eq. (3.4) indicates the meridional Ekman transport integrated in the ocean interior, while the second term represents the meridional geostrophic transport integrated along the characteristic line in the interior.

We note that Eq. (3.2) does not include nonlinear terms. Although one may think that the vorticity flux term violates the Island Rule, this affects the original Island Rule within less than 20% unless the inertial effect is unrealistically large (Pedlosky et al. 1997). Also, the time-averaged vorticity flux is smaller less than the instantaneous one, when the period of the time-average is longer than the period of eddy occurrence. In our analysis, we focus on the low-frequency variability in which the effect of vorticity flux is reduced. Therefore, we may assume that nonlinear terms are negligible. The derivation of the above equations is provided in more detail in Appendix A, and we discuss about effects that are not included in the above equations later.

3.4.2 Application of the TDIR to Madagascar

Applying the TDIR to Madagascar, we obtain the time series of the SBL (Fig. 3.8). In the TDIR, the SBL is definted as the latitude at which the meridional transport becomes zero in the western boundary layer. As shown by Chen et al. (2014), the climatological SBL is well reproduced by the TDIR (Fig. 3.8a), although the mean SBL ($18.1°$S) obtained from the TDIR here is slightly different from $18.3°$S reported by Chen et al. (2014). This small discrepancy may be due to the differences in the wind stress product and the definition of the western boundary layer. Interannual anomalies calculated with the TDIR seems to well reproduce the SBL obtained from the ORAS4 (Fig. 3.8b); the correlation coefficient between these two time series is 0.52, which is significant at the 85% confidence level. The differences between these two time series, especially for high frequency variability, may be due to the topographic effects (such as the Mascarine Ridge located about $10°$ east of the island), mesoscale eddies, higher baroclinic modes, and/or the differences between the phase speeds of the Rossby waves in the TDIR and the ORAS4 that are not included in the TDIR. Nonlinear processes (Trenary and Han 2012) that are not explicitly but implicitly included in the ORAS4 may also contribute to the differences. Although there are some differences, the TDIR can well reproduce the low-passed SBL time series.

Also, the meridional transport anomalies of NEMC (at $14°$S) and SEMC (at $24°$S)

calculated by the TDIR correspond well with those obtained from the ORAS4 (Fig. 3.9). Although there are some differences probably owing to the same reason as at $18°$S, their correlation coefficient for the NEMC (SEMC) transport is 0.74 (0.72 with 3 months lag), which is significant at the 90% confidence level. Therefore, we expect that the TDIR can provide useful insight into the dynamics of interannual variations in the SBL and the western boundary currents along Madagascar.

To investigate the mechanism of the SBL variation, we decompose the transport anomaly within the western boundary layer (T_{bc}) around the mean bifurcation latitude ($18.3°$S in Fig. 3.8a). Figure 3.10 shows the time series of T_{bc} and its components at $18°$S. The seasonal variation of T_{bc} is mainly due to the inflow from the interior and the local transport driven by the wind stress around the island (Fig. 3.10a). This is in agreement with Chen et al. (2014), who obtained the same conclusion using the TDIR, but with a different wind stress data. On the other hand, the interannual anomaly of T_{bc} is mostly a response to the inflow from the interior, and the contribution from the local wind and the storage is very small (Fig. 3.10b). The anomalous inflow from the interior is mainly explained by the meridional interior transport (T_{in}), and partially by the meridional interior transport averaged meridionally (T_{inave}) (Fig. 3.10c). Thus, we can conclude that the interannual SBL anomaly is predominantly determined by the meridional interior transport anomaly.

The mechanism of the NEMC and SEMC variation is almost the same with that of the SBL. The seasonal variations of the NEMC and SEMC transports are mainly due to the inflow from the interior, but significantly modified by the transport driven by the local wind stress and changes in the storage (Figs. 3.11a and 3.12a). Also, the interannual anomalies are due to the anomalous inflow from the interior (Figs. 3.11b and 3.12b). At $14°$S, the inflow from the interior is mostly explained by the T_{in} anomaly (Fig. 3.11c), whereas that from the interior at $24°$S is explained by T_{in}, and modified by T_{inave} mainly after 1995 (Fig. 3.12c).

3.4.3 Sources of variations in the interior transport

To determine the wind stress in which regions are important for the transport variability near Madagascar, we calculate the explained variance ("skill") of the interior transport (Qiu and Chen 2010) as follows:

$$Skill(x,y) = 1 - \frac{< [(T(x,y,t) - \overline{T(x,y,t)}) - (T(x_e,y,t) - \overline{T(x_e,y,t)})]^2 >}{< [T(x_e,y,t) - \overline{T(x_e,y,t)}]^2 >}. \quad (3.5)$$

Here, $T(x,y,t)(= \int_{x_{w+}}^{x} v(x',y,t)Hdx')$ is the meridional transport integrated from the western boundary $(x = x_{w+})$ to x, $T(x_e,y,t)$ corresponds to $T_{in}(y,t)$, $\overline{(...)}$ denotes the time average of each variable, and $<>$ is the sum of each variable.

The explained variance starts to increase rapidly from $60°$E eastward at $18°$S (Fig. 3.13a) (e.g. the explained variance increases by 0.55 from $60°$E to $80°$E) (Fig. 3.13a, red lines), owing to the geostrophic term (Fig. 3.13c), which shows a similar rapid increase, rather than the Ekman term (Fig. 3.13b). The geostrophic term is not determined by the instantaneous wind stress on the same latitude, but the wind stress along the characteristic line, while the Ekman term depends on the instantaneous wind stress. Therefore, the westward propagating signal generated by wind stress curl may be canceled out by wind stress curl of the opposite sign in other seasons, and most of the signals reaching Madagascar are from the west of $90°$E. The explained variance at $14°$S ($24°$S) is similar to that at $18°$S, except that the rapid increase occurs further to the east (west).

3.5 Possible connection with ENSO

3.5.1 Correlation analyses

To find out whether the interannual variations discussed in the previous subsections are related to large-scale climate modes such as the ENSO and the IOD, we first compare interannual variations of the SBL and the NEMC and SEMC transports with the Niño 3.4 index and the Dipole Mode Index (DMI) (Fig. 3.14). The Niño 3.4 index is defined as an

average of SST anomalies over the Niño 3.4 region (120°W-170°W, 5°S-5°N), while the DMI is computed by taking the difference in SST anomalies between the western tropical Indian Ocean (50°E-70°E, 10°S-10°N) and the south-eastern tropical Indian Ocean (90°E-110°E, 10°S-Equator). Although both indices are correlated with the SBL and the NEMC and SEMC transport anomalies (Figs. 3.14b, c), the Niño 3.4 index is more strongly correlated (Figure not shown). For example, the maximum correlation coefficient between SBL and DMI is lower than -0.3, which is not significant at the 90% confidence level. The correlation with the DMI may be due to the positive correlation between the Niño 3.4 index and the DMI (Yamagata et al. 2004). This is consistent with Rao and Behera (2005), who suggested that westward propagating Rossby waves to the south (north) of 10°S are predominantly forced by the ENSO (IOD) based on partial correlation analyses. Thus, we focus on the relation with the ENSO for the rest of this study.

To examine the relation with the ENSO more closely, we calculate the sliding lag-correlation coefficient with the Niño 3.4 index (Fig. 3.15). Although the correlation undergoes decadal variations, relatively strong positive (negative) lag-correlation is found between the SBL (NEMC and SEMC transports) and the Niño 3.4 index with the maximum correlation at around 10-15 (5-15) months lag in the latter period. This suggests that the interannual variations in the SBL and the NEMC and SMEC transports may be related to wind stress anomalies associated with the ENSO. If this time lag is due to the Rossby wave propagation from the interior to Madagascar and their phase speed is about 0.10 m/s, these Rossby waves are generated around 60°E-90°E, in agreement with the source region shown in Section 3.4.3. We note that the statistically insignificant correlation in the earlier period (Figs. 3.14a,c,d) may be due to an abnormal event in 1982/83 (Tozuka et al. 2014a) and/or the assimilation of the SSH in the recent period.

3.5.2 Wind stress curl anomaly associated with ENSO

To check whether the ENSO can generate wind stress curl anomalies in the above region, we first apply the empirical orthogonal function (EOF) analysis to wind stress curl

anomalies over the southern Indian Ocean (Fig. 3.16a). The first EOF mode shows a meridional dipole pattern with a positive peak in the central tropical Indian Ocean around $80°$E, $13°$S and a negative peak to the southeast of Madagascar. The spatial pattern is similar to that of Zhuang et al. (2013), but their northern peak was located around $90°$E. The slight difference may be because we analyzed a different period of the data. Since the principal component of the first EOF mode (PC1) and the Niño 3.4 index correspond well with each other (Fig. 3.16b) with their correlation coefficient of 0.57 (significant at the 90% confidence level), the above wind stress curl anomalies may be related to the ENSO.

Next, to construct the time series of the dominant mode of wind stress curl anomalies in the southern Indian Ocean, we define the time series of $curl\ \tau$ (black line in Fig. 3.16b) as wind stress curl anomalies averaged over $70°$E-$90°$E, $20°$S-$10°$S (Box in Fig. 3.16a). In this time series, seven maxima above one standard deviation (minima below minus one standard deviation) are found: Aug. 1986, Feb. 1988, Sep. 1991, Aug. 1994, Jan. 1998, Jun. 2003, and Jul. 2006 (Jul. 1984, May. 1989, Nov. 1996, Jun. 2000, Jan. 2002, Jun. 2010, and Jun. 2012) (Fig. 3.16b).

We then construct composites to examine large-scale anomaly fields during the positive (negative) events of wind stress curl anomalies (Figs. 3.17, 3.18). Anticyclonic (Cyclonic) anomalies associated with significant positive (negative) SLP anomalies are seen to the northwest of Australia (Figs. 3.17a, 3.18a). Also, the positive (negative) events appear to co-occur with El Niño (La Niña) (Figs. 3.17b, 3.18b). Note that significant SST anomalies associated with the IOD are not seen. From these results, we may conclude that the wind stress curl anomalies induced by the ENSO to the northwest of Australia generate the interannual variations in the western boundary currents along the Madagascar coast and the SBL.

These SLP and wind stress anomalies may partly be explained by the Matsuno-Gill response (Matsuno 1966; Gill 1980) to diabatic heating anomalies in the tropical Pacific associated with the ENSO (Tozuka et al. 2014a). This is supported by precipitation anomalies, a good indicator of diabatic heating anomalies, in the tropical Pacific (Figs.

3.17c, 3.18c). Furthermore, these anomalies in this area may be modified by positive (negative) SST anomalies associated with Ningaloo Niño (Niña) (Fig. 3.18b), which often co-occurs with La Niña (El Niño) (Kataoka et al. 2014; Tozuka et al. 2014a). Ningaloo Niño (Niña) events associated with positive (negative) SST anomalies off the west coast of Australia are often triggered by downwelling (upwelling) coastal waves originating from the western Pacific during La Niña (El Niño). These positive (negative) SST anomalies generate negative (positive) SLP anomalies in the overlying atmosphere through the local air-sea interaction.

3.6 AGCM sensitivity experiments

To verify the mechanism of wind stress anomalies in the interior region of the southern Indian Ocean proposed in the previous subsection, we conduct atmospheric general circulation model (AGCM) sensitivity experiments.

3.6.1 AGCM

We use outputs from an AGCM called the Frontier Atmospheric General Circulation Model (FrAM; Guan et al. 2000; Tozuka et al. 2014b) to investigate the possible influence of ENSO and Ningaloo Niño on the wind stress curl field in the Indian Ocean. This AGCM is the atmospheric component of the University of Tokyo Coupled general circulation model (Tozuka et al. 2006, 2011; Doi et al. 2010), and capable of reproducing atmospheric anomalies associated with IOD and ENSO over the Indian Ocean (Yuan et al. 2012; Tozuka et al. 2014a). The governing equations are transformed into spectral forms with triangular truncation at wavenumber 42, corresponding to the zonal resolution of 2.8125°. The model has 28 hybrid levels in the vertical direction from the surface up to 10 hPa isobaric surface. Among three cumulus convection schemes implemented in the FrAM, that developed by Emanuel (1991) is used. More details of this AGCM can be found in Guan et al. (2000) and Tozuka et al. (2014b).

In this study, two experiments with five ensemble members are conducted. In the control (CTL) run, monthly SST and sea ice cover observed in 1950-2011 are used to force the model. To examine the influence of the ENSO and Ningaloo Niño on the wind pattern in the Indian Ocean, we conducted the TROPAC and ESIO experiments, in which SST is allowed to vary interannually only in the tropical Pacific and southeastern Indian Ocean, respectively (Fig. 3.19), and the monthly climatology of SST is prescribed elsewhere. To reduce the effect of artificial discontinuity of SST in the tropical Pacific, the imposed SST anomalies are linearly decreased poleward near the northern/southern boundary of interannually varying SST region. We analyzed the outputs from 1980 to 2009 to be compatible with the reanalysis data.

3.6.2 Tropical Pacific vs southern Indian Ocean

To quantify the contribution of the tropical Pacific and southeastern Indian Ocean, we regress area-averaged wind stress curl anomaly in the interior of the southern Indian Ocean ($60-90°$E, $10-20°$S) to the ensemble mean of anomalous SLP field in each experiment as well as the reanalysis data. Comparing spatial pattern of regression coefficients in the CTL run and ERA-Interim, we find that the CTL experiment reproduce SLP anomalies well (Figs. 3.20a, b). Although the amplitude of the CTL run is slightly large compared to the ERA-Interim, positive anomalies off the northwestern coast of Australia can be seen in both.

A comparison between the CTL and TROPAC experiments enables us to quantify the relative contribution of the interannual tropical Pacific forcing (Figs. 3.20b, c). In the TROPAC experiments, a Rossby wave-like pattern can be found in the northwestern Pacific and the southeastern Indian Ocean more clearly than the CTL run. This is attributed to the Matsuno-Gill response to the diabatic heating anomaly in the western tropical Pacific (Feng et al. 2013; Tozuka et al. 2014a). Since the amplitude of the regression coefficients is almost the same in the southern Indian Ocean in the TROPAC and CTL experiments, the interannual tropical Pacific forcing can effectively generate wind stress

anomalies which influence the western boundary currents along Madagascar.

Similarly, anticyclonic anomalies off the western coast of Australia are also significant in the ESIO experiment, although the amplitude of the anomalous anticyclone is smaller than the CTL and TROPAC experiments (about 50%; Figs. 3.20c, d). These anomalies are generated by local SST anomalies associated with Ningaloo Niño (Kataoka et al. 2013; Tozuka et al. 2014a). Negative anomalies in the southwestern Indian and the Southern Oceans are small or insignificant since there is no atmospheric teleconnection (i.e. Pacific-South Atlantic pattern; Mo 2000) induced by the ENSO. The ESIO experiment indicates that interannual variability of the SST in the southeastern Indian Ocean can explain about half of the wind stress curl anomalies in the interior even without the influence of the ENSO.

In conclusion, positive (negative) SLP anomalies off the northwestern coast of Australia are generated by the Matsuno-Gill response to the El Niño (La Niña), and thus positive (negative) wind stress curl anomalies in the interior. Although Ningaloo Niña (Niño) sometimes co-occurs with El Niño (La Niña) (e.g. Fig. 3.18), relevant negative (positive) SST anomalies also makes positive (negative) SLP and wind stress curl anomalies. Thus, wind stress curl anomalies which affect the western boundary currents along Madagascar are mainly due to the response to the ENSO and partly due to amplification by the local air-sea interaction.

3.7 Further considerations

Although it takes more than a year for Rossby waves to cross the southern Indian Ocean (e.g. Perigaud and Delecluse 1993), effects of damping are not included in the TDIR used in Sect. 3.4. Also, Rossby waves are radiated from the west coast of Australia (Li and Clarke 2004) and the Indonesian Throughflow is known to influence circulation in the southern Indian Ocean (Hirst and Godfrey 1993), but these eastern boundary influences are not included in the TDIR. Thus, we extend the TDIR by incorporating the above

effects.

The equations for the upper layer thickness anomaly, meridional interior transport, and western boundary current transport can be rewritten as

$$\begin{aligned} h(x,y,t) &= \frac{1}{C_R}\int_{x_e}^{x} B(x',y,t-\frac{x-x'}{C_R})\exp[\frac{\epsilon}{C_R}(x'-x)]dx' \\ &\quad +h(x_e,y,t-\frac{x-x_e}{C_R})\exp[\frac{\epsilon}{C_R}(x'-x)], \end{aligned} \tag{3.6}$$

$$\begin{aligned} T_{in}(y,t) &= \int_{x_e}^{x_{w+}}\frac{\tau^x}{f\rho_0}dx' \\ &\quad -\frac{Hg'}{C_R f}\int_{x_e}^{x_{w+}} B(x',y,t-\frac{x-x'}{C_R})\exp[\frac{\epsilon}{C_R}(x'-x_{w+})]dx' \\ &\quad +\frac{g'H}{f}\{h(x_e,y,t)-h(x_e,y,t-\frac{x_{w+}-x_e}{C_R})\}\exp[\frac{\epsilon}{C_R}(x_e-x_{w+})], \end{aligned} \tag{3.7}$$

and

$$\begin{aligned} T_{bc}(y,t) &= -T_{in}(y,t)+\frac{1}{\Delta y}\int_{y_s}^{y_n} T_{in}(y,t)dy \\ &\quad +\frac{1}{\Delta y}\oint_{C_1}\frac{\boldsymbol{\tau}(t)\cdot d\boldsymbol{I}}{\rho_0\beta} \\ &\quad +\int_{y}^{y_n}\int_{x_{w+}}^{x_e}\frac{\partial h}{\partial t}dxdy-\frac{1}{\Delta y}\int_{y_s}^{y_n}\int_{x_{w+}}^{x_e}(y-y_s)\frac{\partial h}{\partial t}dxdy \\ &\quad -\frac{1}{\Delta y}\int_{CBA}(y-y_s)H(\boldsymbol{k}\times\boldsymbol{u})\cdot d\boldsymbol{I}+\int_{BA}H(\boldsymbol{k}\times\boldsymbol{u})\cdot d\boldsymbol{I}, \end{aligned} \tag{3.8}$$

respectively. Here, ϵ is the Newtonian dissipation coefficient, and we used $2\ year^{-1}$ following Zhuang et al. (2013). Also, $\boldsymbol{k}$ is the unit vector normal to the integral path, $\boldsymbol{u}$ indicates the velocity vector, and other notations are the same with Eqs. (3.1)-(3.4). The terms on the fourth line of Eq. (3.8) indicate the volume inflow from the eastern boundary (i.e. Indonesian Throughflow). We use velocity data of the ORAS4 for the horizontal velocity at the eastern boundary. Also, to represent the upper layer thickness anomaly at the eastern boundary, we use the $15°\mathrm{C}$ isotherm (D15 anomaly), because the mean D15

is close to the mean upper layer thickness (H) in the TDIR.

3.7.1 Eastern boundary forcing

When the upper layer thickness is calculated based on Eq. (3.6), instead of Eq. (3.3), it is found that the effects of the eastern boundary are confined to the eastern Indian Ocean (figure not shown). This supports the earlier studies (e.g. Masumoto and Meyers 1998), which examined interannual Rossby waves in the southern Indian Ocean. Furthermore, the seasonal and interannual variations of T_{bc} do not change much even when the effects of the eastern boundary are included in the TDIR (figure not shown). This is because the large inflow from the Indonesian Throughflow is found mostly to the north of $13°$S, and the inflow is relatively small in the latitudinal band of Madagascar from $25°$S to $13°$S. Since Chen et al. (2014) showed that the Indonesian Throughflow does not significantly change the seasonal variation of the SBL, the effects of eastern boundary on the western boundary currents are small for seasonal-to-interannual time scales.

3.7.2 Damping effect

In contrast to the eastern boundary effects, the damping term alters the seasonal and interannual variations of the western boundary current transport. The mean T_{bc} changes from 20 Sv to 12 Sv at $14°$S, from 0.88 Sv to -1.3 Sv at $18°$S, and from -18 Sv to -10 Sv at $24°$S when the damping term is included (Fig. 3.21). Also, the amplitudes of seasonal and interannual variations in T_{bc} at $14°$S, $18°$S, and $24°$S are reduced compared to the case without the damping term (Fig. 3.21). The standard deviation of the seasonal variation reduces 15% at $14°$S, 43% at $18°$S, and 21% at $24°$S, while that of interannual anomalies reduces 27% at $14°$S, 33% at $18°$S, and 48% at $24°$S. These reductions in T_{bc} are due to the reduced inflow from the interior. This may be because the westward propagating signals generated by Ekman pumping in the central South Indian Ocean are damped during their propagation and these weaker signals result in smaller meridional transport in the interior. However, we emphasize that the mechanisms presented in Sect. 3.4 are robust

even though the damping term reduces the amplitude of T_{bc}.

3.7.3 Nonlinearity

Here, we estimate the nonlinear term, which may affect the Island Rule (Eq. A17). Since the resolution of the ORAS4 is not high enough to calculate the vorticity flux associated with eddy activity, we use the AVISO geostrophy.

Figure 3.23 shows interannual anomalies of NEMC, SEMC and the nonlinear term, i.e. $-\frac{H}{\beta\Delta y}\oint_{C_1}(\boldsymbol{u}\cdot\nabla)\boldsymbol{u}\cdot d\boldsymbol{l}$. Although the amplitude of NEMC and SEMC is different from that in the ORAS4 (Fig. 3.3) due to the use of surface geostrophic current, transport anomalies driven by the nonlinear term is much smaller than the NEMC and SEMC transport. This indicates that the nonlinearity associated with eddy shedding plays a relatively minor role and the qualitative results presented in Sect. 3.4 remain the same.

3.8 Summary

In this chapter, interannual variability of the SBL and seasonal and interannual variability of the volume transport of the western boundary currents (i.e., NEMC and SEMC) along the Madagascar coast are first investigated using observational and reanalysis data. We have found that the interannual variations of the NEMC (SEMC) transport are more closely linked with those of the SEC transport than those of the SBL, and influence relative vorticity at the northern (southern) edge of Madagascar, which is the main vorticity source region for the downstream regions.

Then, the dynamical mechanisms of interannual variations in the SBL and the NEMC and SEMC transports are investigated using the TDIR (Firing et al. 1999; Chen et al. 2014). For this purpose, the original TDIR is extended to include effects of dissipation in westward propagating Rossby waves, the eastern boundary conditions, and the nonlinearity associated with eddy shedding. Although some differences are found probably owing to topographic effects, mesoscale eddies, higher baroclinic modes, the phase speed

of the Rossby waves, and/or nonlinear processes, the TDIR can reproduce not only the seasonal variations of the SBL, but also its interannual variations. When contributions from different terms in the TDIR are examined, it is found that the meridional transport anomaly in the ocean interior induced by anomalous wind stress curl at 60°E-90°E in the same latitudinal band plays the key role in the interannual variations of the SBL. The interannual variations in the NEMC and SEMC transports are also due to the meridional transport anomaly in the ocean interior. Although the dynamical mechanism of the seasonal variation in the SBL has already been shown by Chen et al. (2014), this study is the first to demonstrate the dynamical mechanisms of the interannual variation in the SBL and the seasonal and interannual variations in the NEMC and SEMC transport using the TDIR.

The above interannual variations are correlated with the ENSO with a phase lag of 5-15 months. We have shown that diabatic heating anomalies associated with the ENSO may generate wind stress curl anomalies over the southern Indian Ocean, and they are modified by the local process in the southeastern Indian Ocean from the statistical analysis of reanalysis data. Furthermore, AGCM sensitivity experiments support these results.

We have also discussed effects of damping, the eastern boundary, and nonlinearity in the TDIR. Although the damping term has an impact on the amplitude of seasonal and interannual variation in the SBL and the NEMC and SEMC transports, it does not affect the above mechanism. Also, we have shown that the eastern boundary effect (i.e. ITF) does not influence the NEMC and SEMC transports. This may be because the ITF mostly influences regions north of the northern tip of Madagascar, and agrees with Le Bars et al. (2013), who reported that the impact of the ITF is mainly compensated by the transport through the Mozambique Channel. Furthermore, the nonlinearity associated with eddy shedding at the northern and southern tips of Madagascar plays a relatively minor role.

Figures

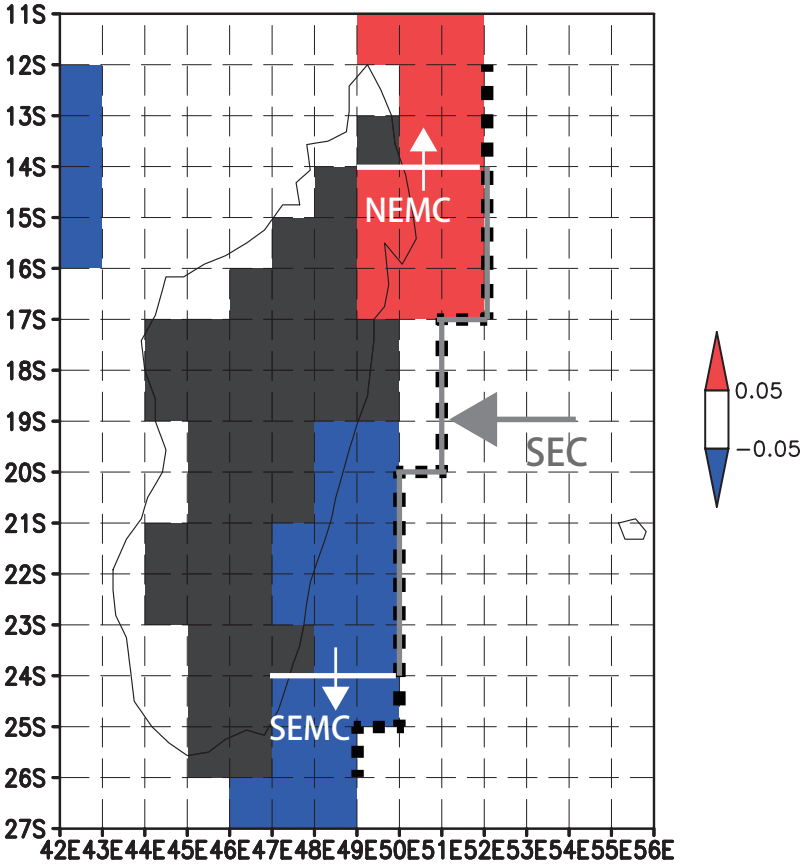

Figure 3.1: The western boundary layer along Madagascar and the annual mean of 400 m depth mean meridional velocity in the ORAS4 (in $m\ s^{-1}$). The western boundary layer is between black dashed line and the Madagascar coast. White (gray) lines indicate the line at which the NEMC and SEMC (SEC) transports are calculated.

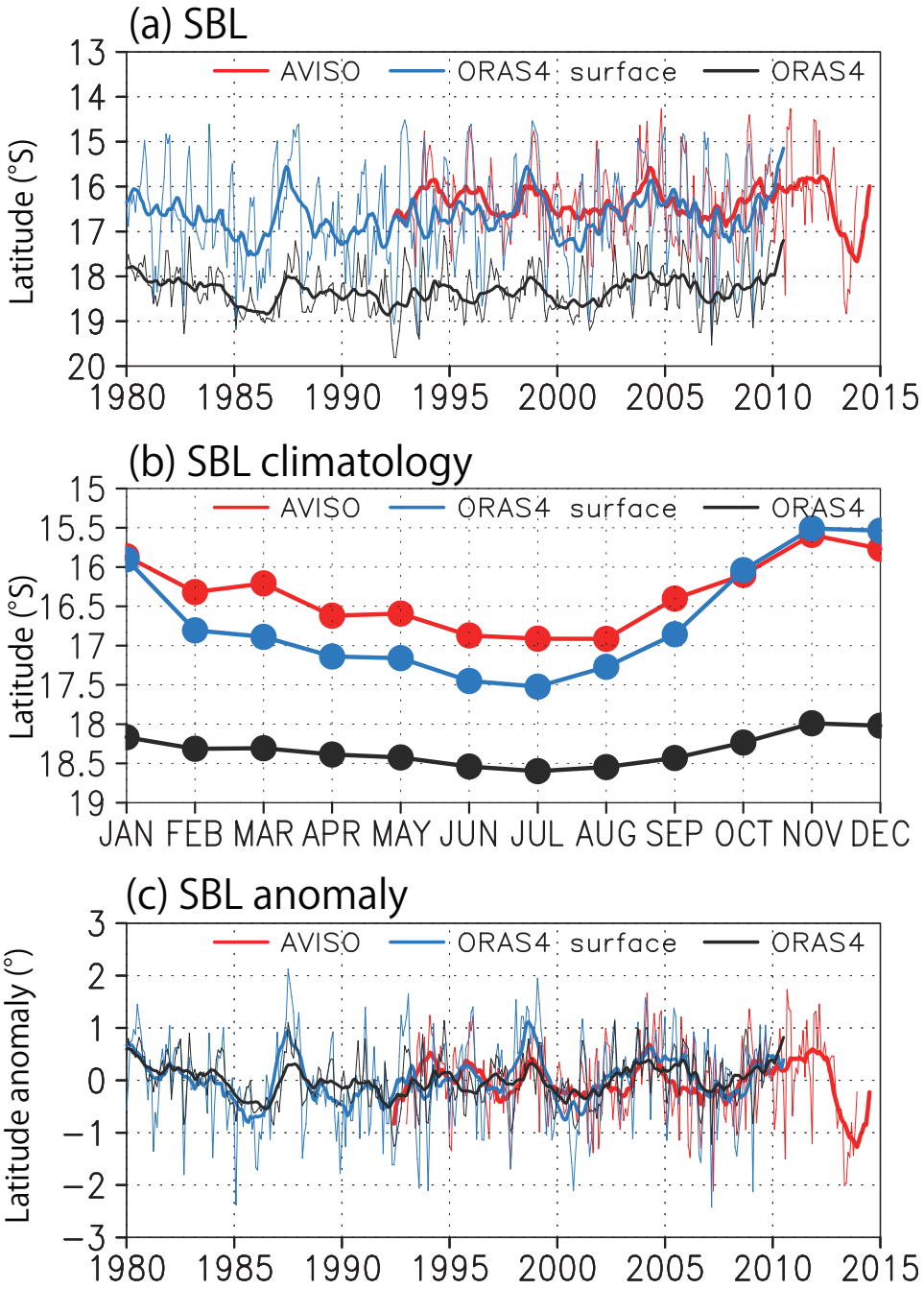

Figure 3.2: (a) Raw time series of the SBL calculated from the AVISO geostrophy (red) and, the surface (blue) and 400 m depth-mean (black) current of the ORAS4. (b) As in (a), but for the climatological SBL. (c) As in (a), but for the interannual SBL anomaly (i.e., (a) minus (b)). The thin lines indicate the monthly mean values, while the thick lines indicate their 15-month running mean.

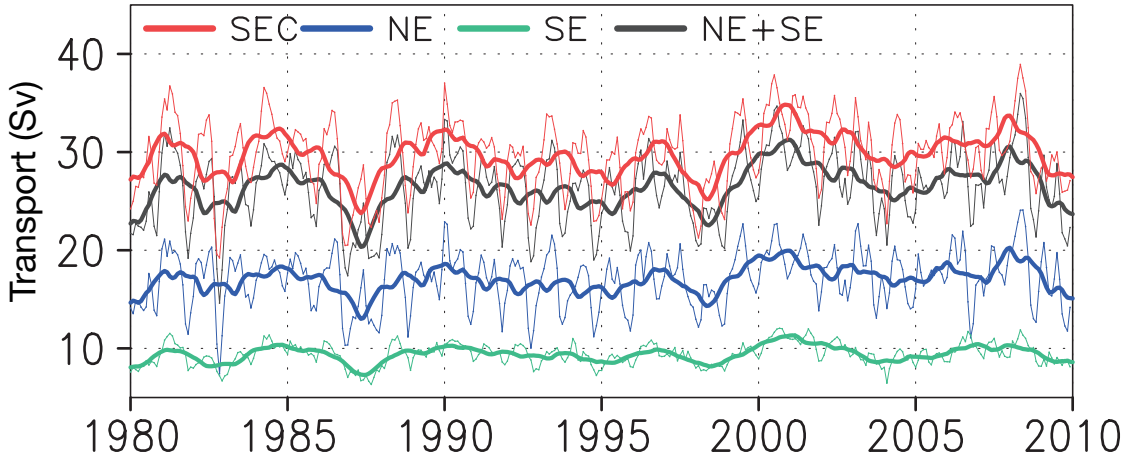

Figure 3.3: Time series of the SEC transport across the gray line in Fig. 3.1 (red), the NEMC transport across $14°$S (NE, blue), the SEMC transport across $24°$S (SE, green), and the sum of NE and SE (gray). The vertical axis is in Sv ($= 10^6 m^3/s$). The thin lines indicate the monthly mean values, while the thick lines indicate their 15-month running mean.

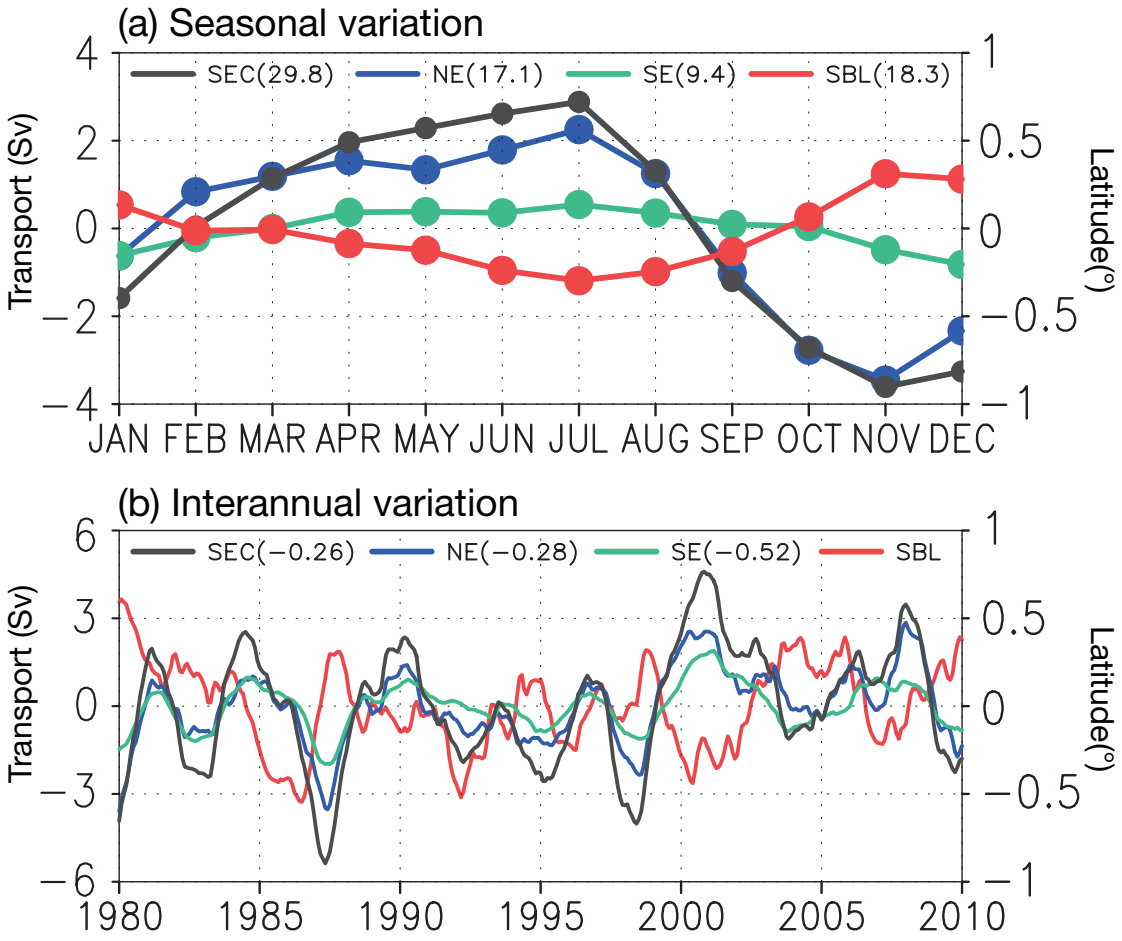

Figure 3.4: (a) Time series of the seasonal anomaly from the annual mean of SBL (red), NE (blue), SE (green), and the SEC transport (gray) in the ORAS4. The vertical axis in the left indicates the transport anomaly (Sv), while the axis in the right shows the bifurcation latitude anomaly (°). The value in the brackets is an annual mean of each variables. Positive values of NE signify northward transport, while those of SE signify southward transport. (b) As in (a), but for interannual anomaly. To show the time series more clearly, only 15-month running means are shown. The value in the brackets is a correlation coefficient between each variable and the SBL.

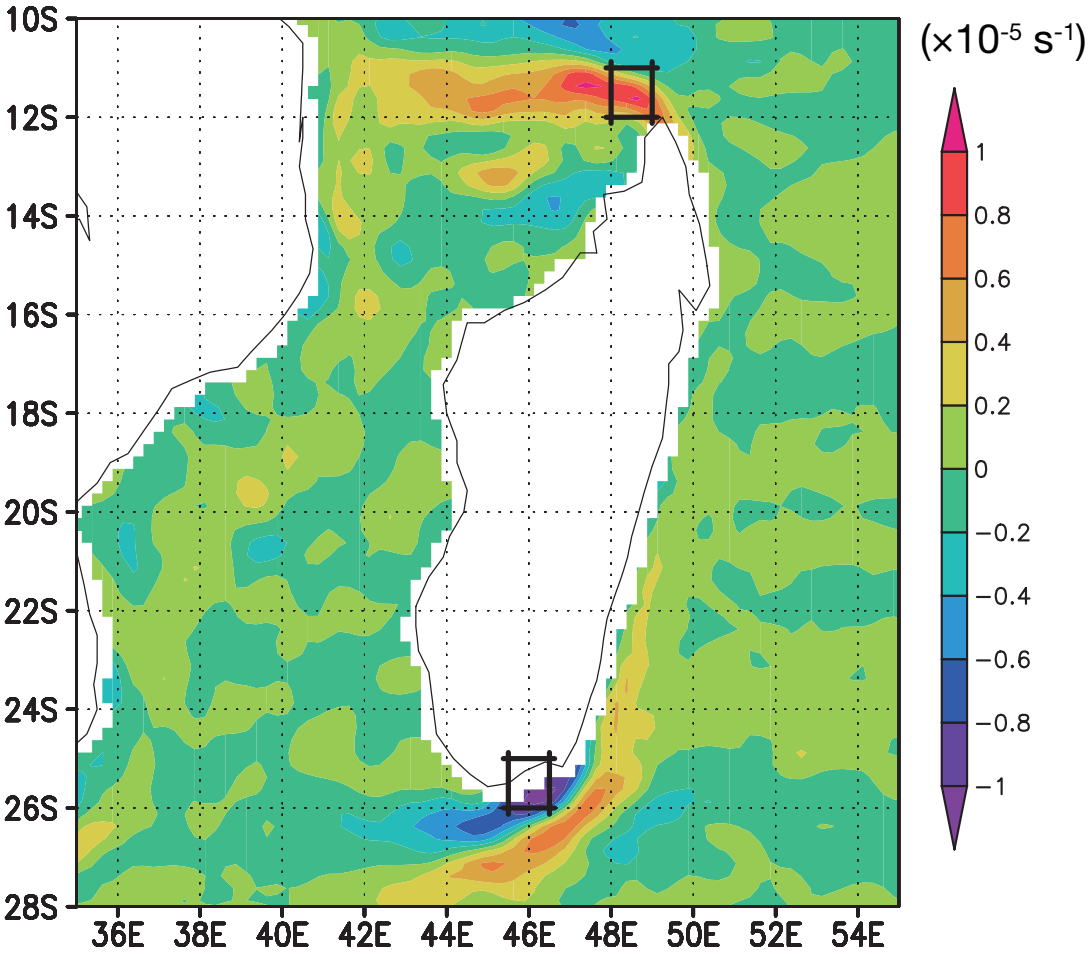

Figure 3.5: Annual mean relative vorticity $[\times 10^{-5} s^{-1}]$ calculated from the AVISO geostrophy from Jan. 1993 to Dec. 2013. The boxes at the northern and southern tips of Madagascar indicate the area in which the vorticity shown in Fig. 3.6 are computed. The relative vorticity are calculated only over ocean grids in each box.

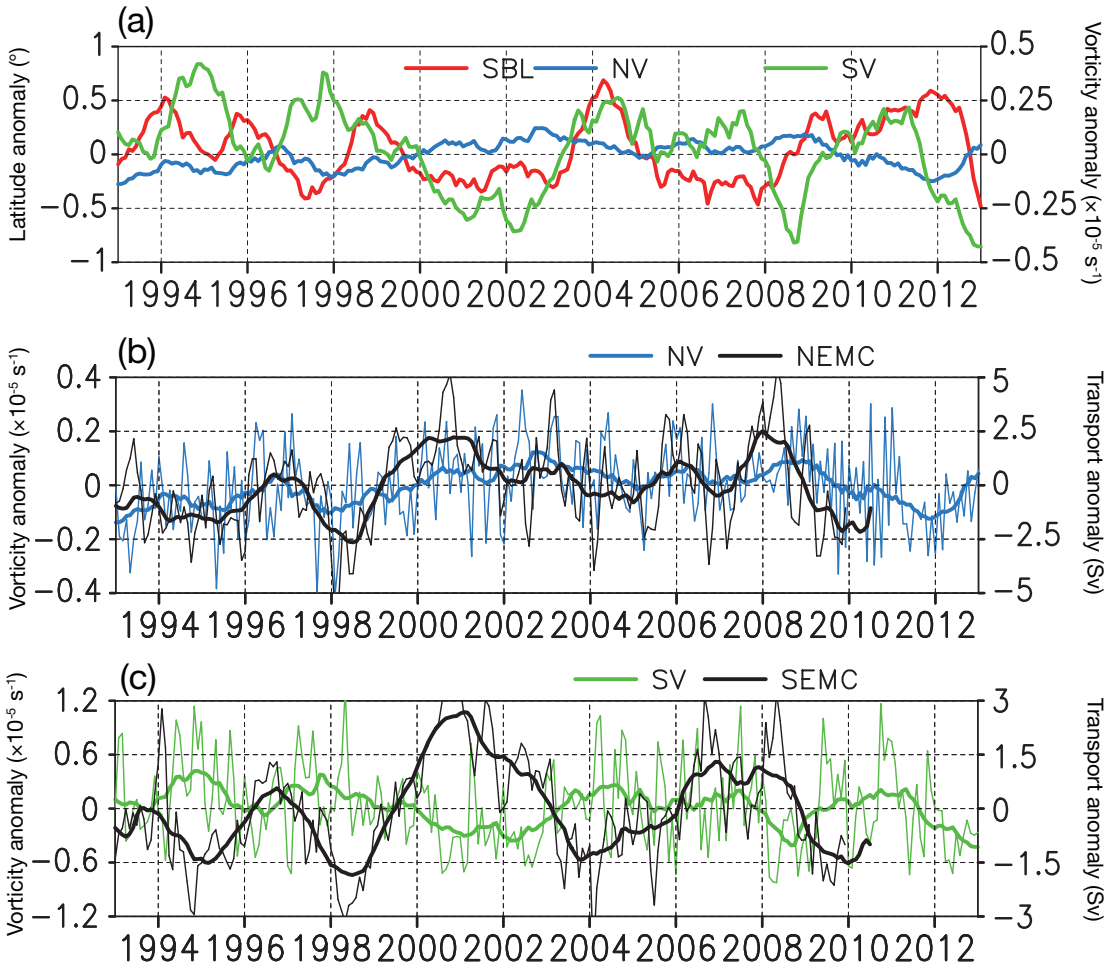

Figure 3.6: (a) Time series of the low-passed SBL anomaly (red), and the vorticity anomaly in the northern (NV; blue) and southern (SV; green) boxes. (b) As in (a), but for NV (blue) and the NEMC transport across 14°S (black). The thin lines indicate the interannual anomalies. (c) As in (b), but for SV (green) and the SEMC transport across 24°S (black). The SBL, NV and SV are calculated from the AVISO geostrophy, while the NEMC and SEMC transports are computed using the ORAS4.

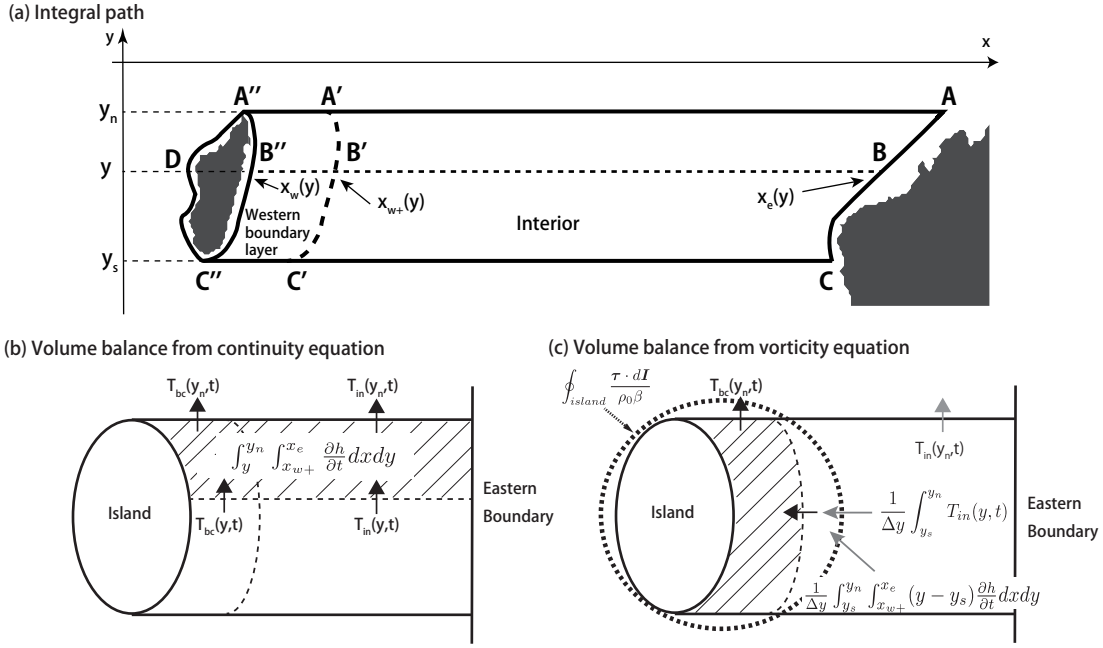

Figure 3.7: Schematic diagram of (a) the integral path of the TDIR, (b) the volume balance from the continuity equation, and (c) the vorticity balance within the western boundary layer.

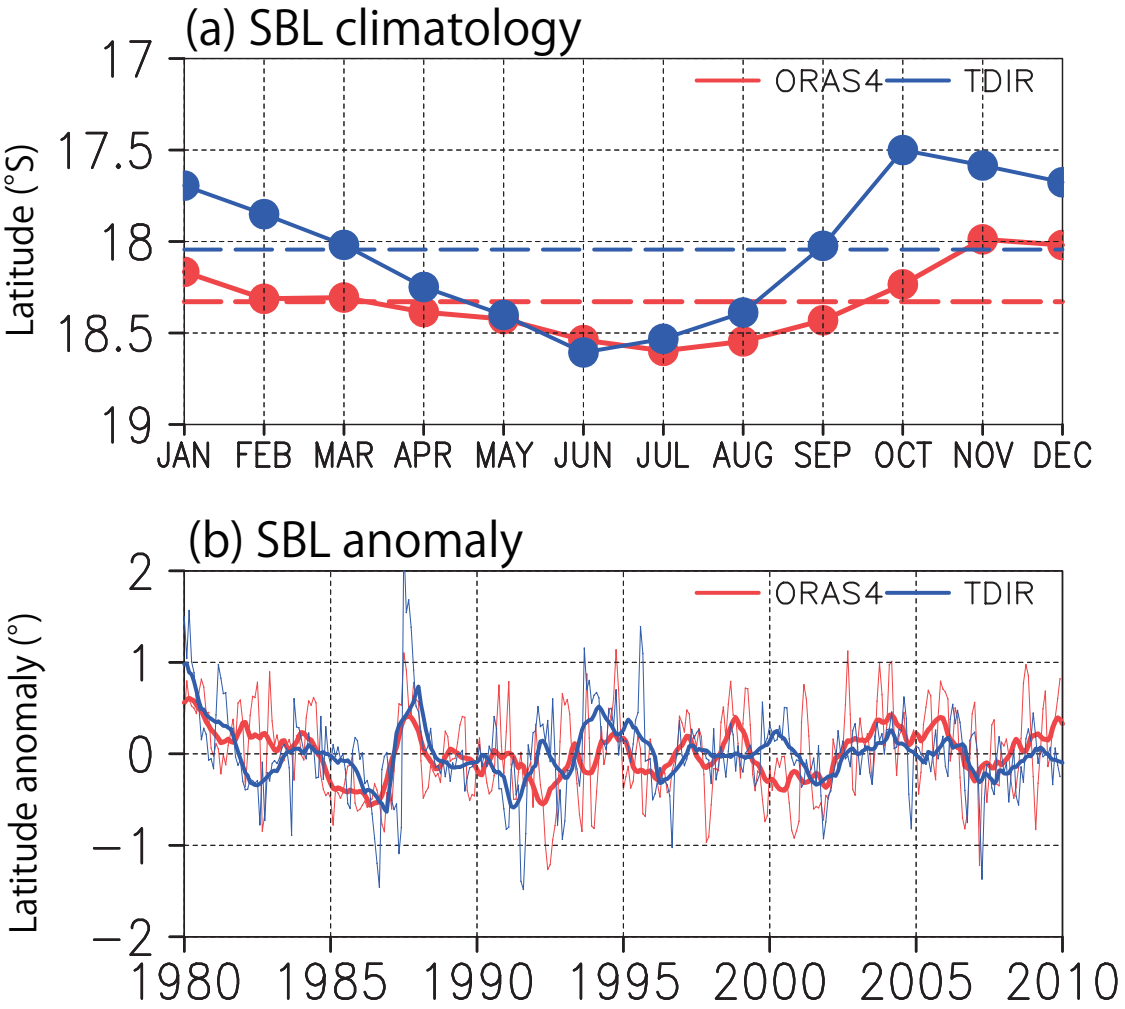

Figure 3.8: (a) Time series of climatological SBL (°) from the ORAS4 (red) and the TDIR (blue). The horizontal dashed lines indicate the mean SBL. (b) As in (a), but for interannual anomalies. The thin lines indicate the monthly anomaly, while the thick lines indicate a 15-month running mean.

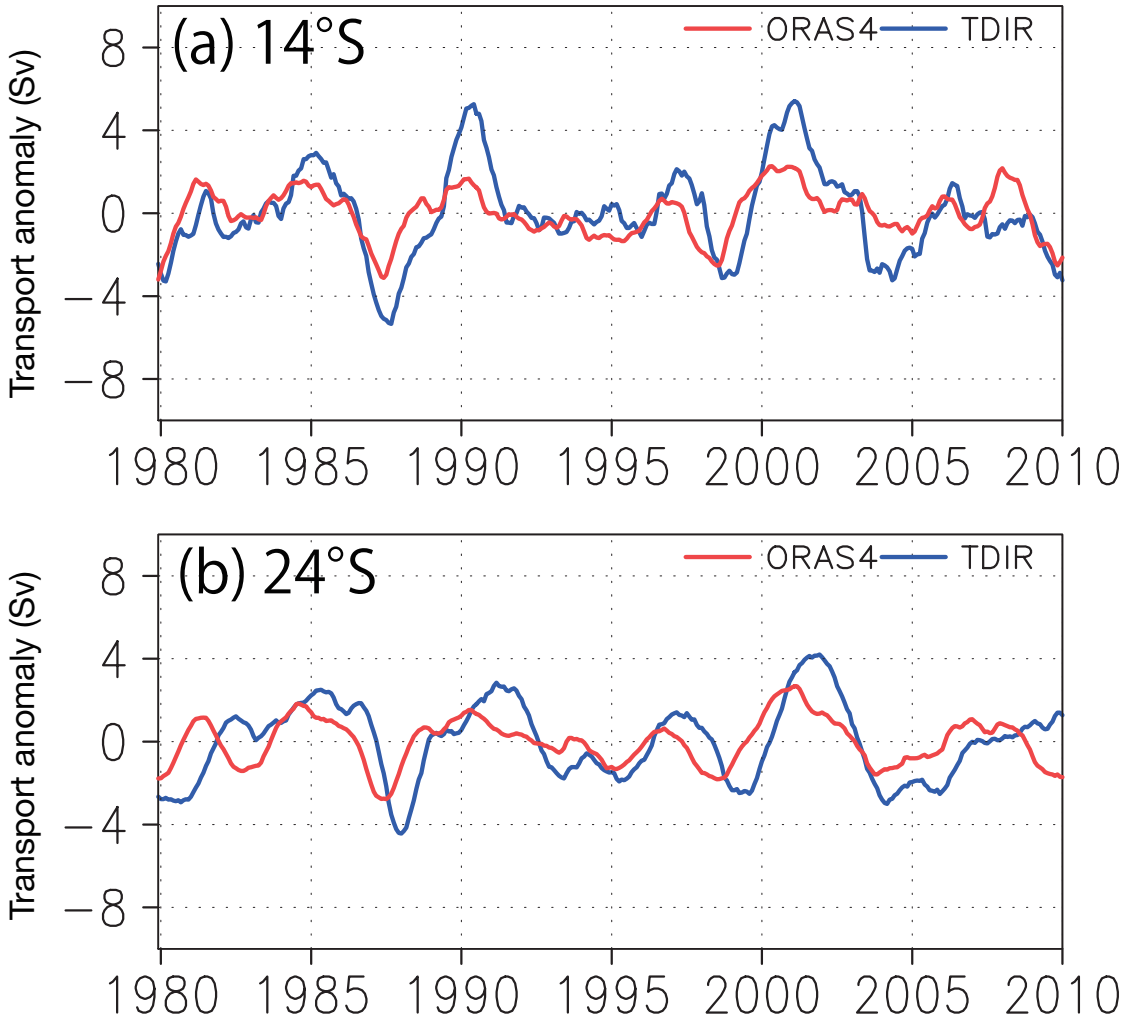

Figure 3.9: (a) NEMC transport anomaly at $14°$S calculated from the ORAS4 (red) and the TDIR (blue). All time series are smoothed with a 15-month running mean and detrended. (b) As in (a), but for the SEMC transport anomaly at $24°$S.

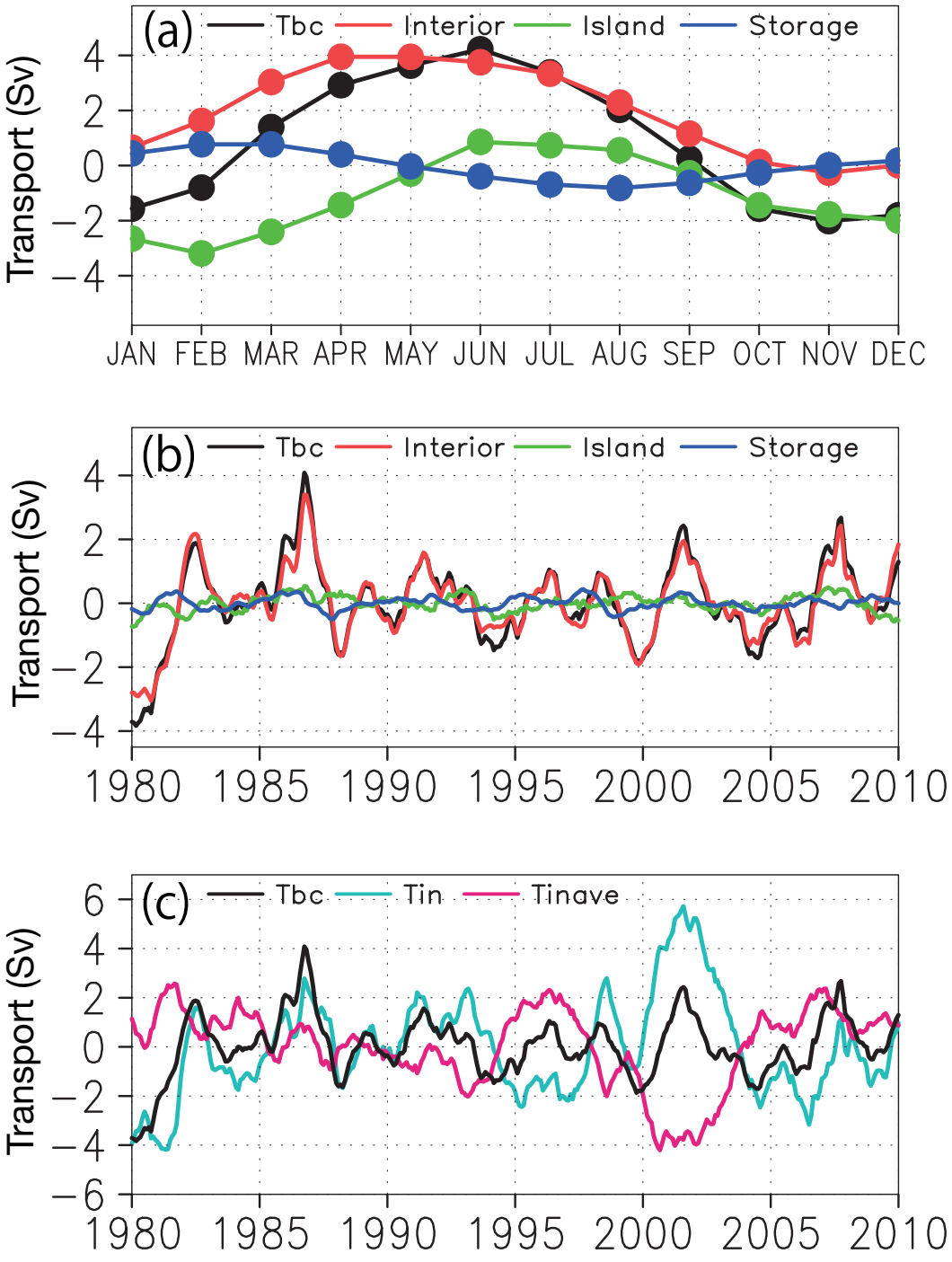

Figure 3.10: Time series of each term in Eq. (2) at 18°S. (a) Seasonal time series of T_{bc} (black), the inflow from the ocean interior (Interior; red), the transport driven by local winds (Island; green), and the storage (Storage; blue). (b) As in (a), but the interannual anomalies. (c) Time series of T_{bc} (black), the meridional transport anomaly in the interior (T_{in}; cyan), and the meridionally averaged T_{in} anomaly (T_{inave}; light red). Interannual anomalies are smoothed with a 15-month running mean and detrended.

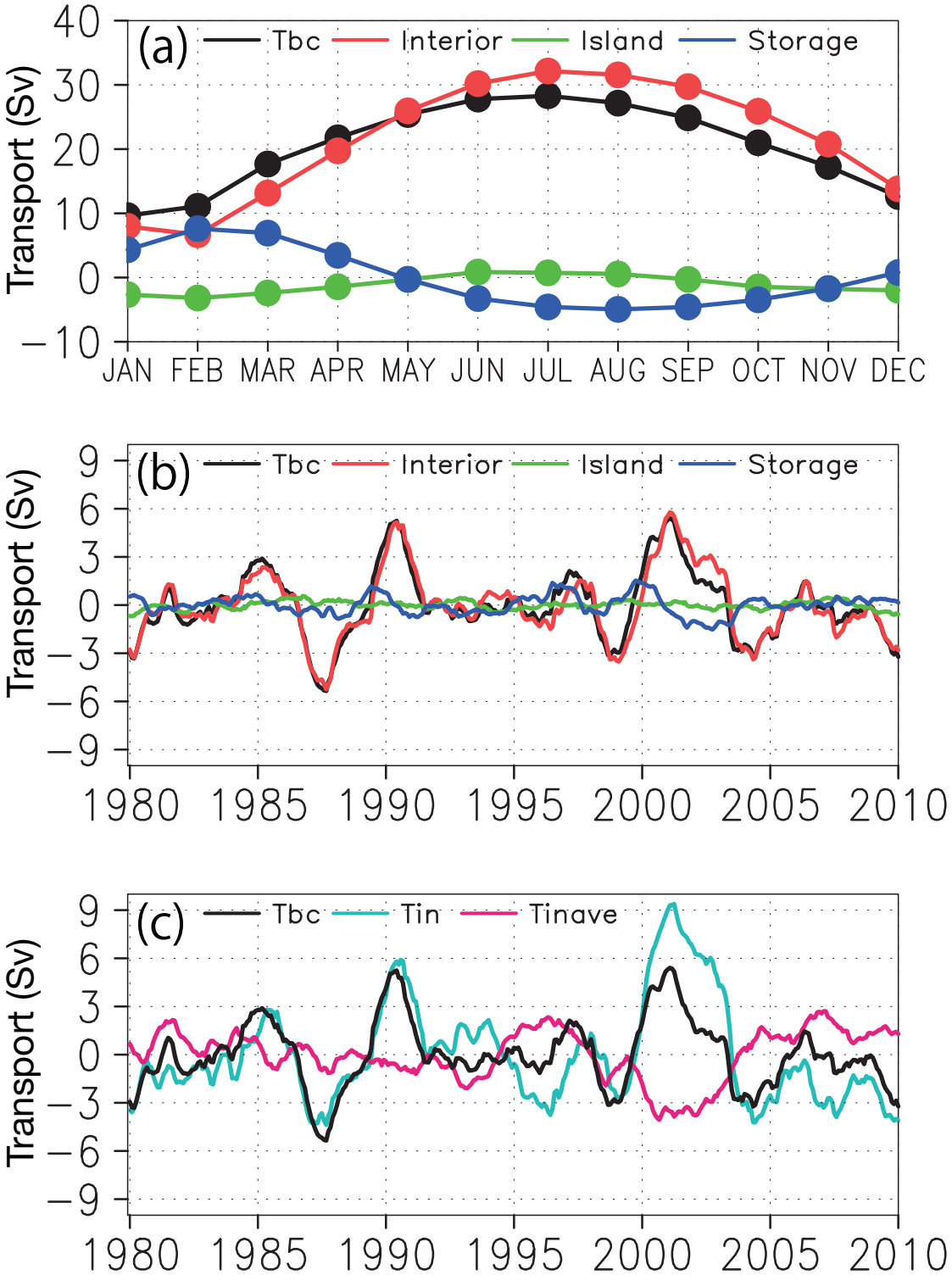

Figure 3.11: As in Fig. 3.10, but at 14°S.

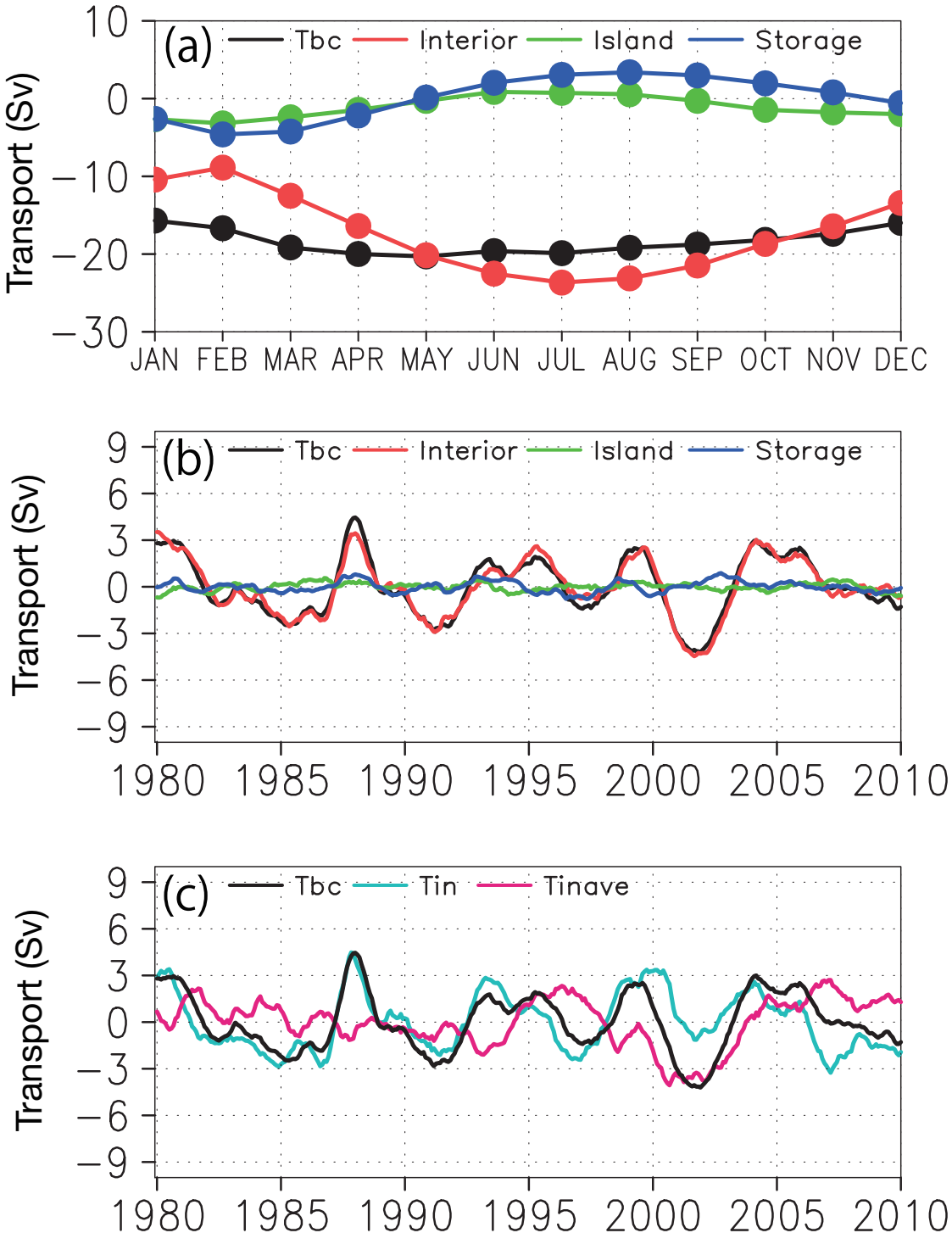

Figure 3.12: As in Fig. 3.10, but at 24°S.

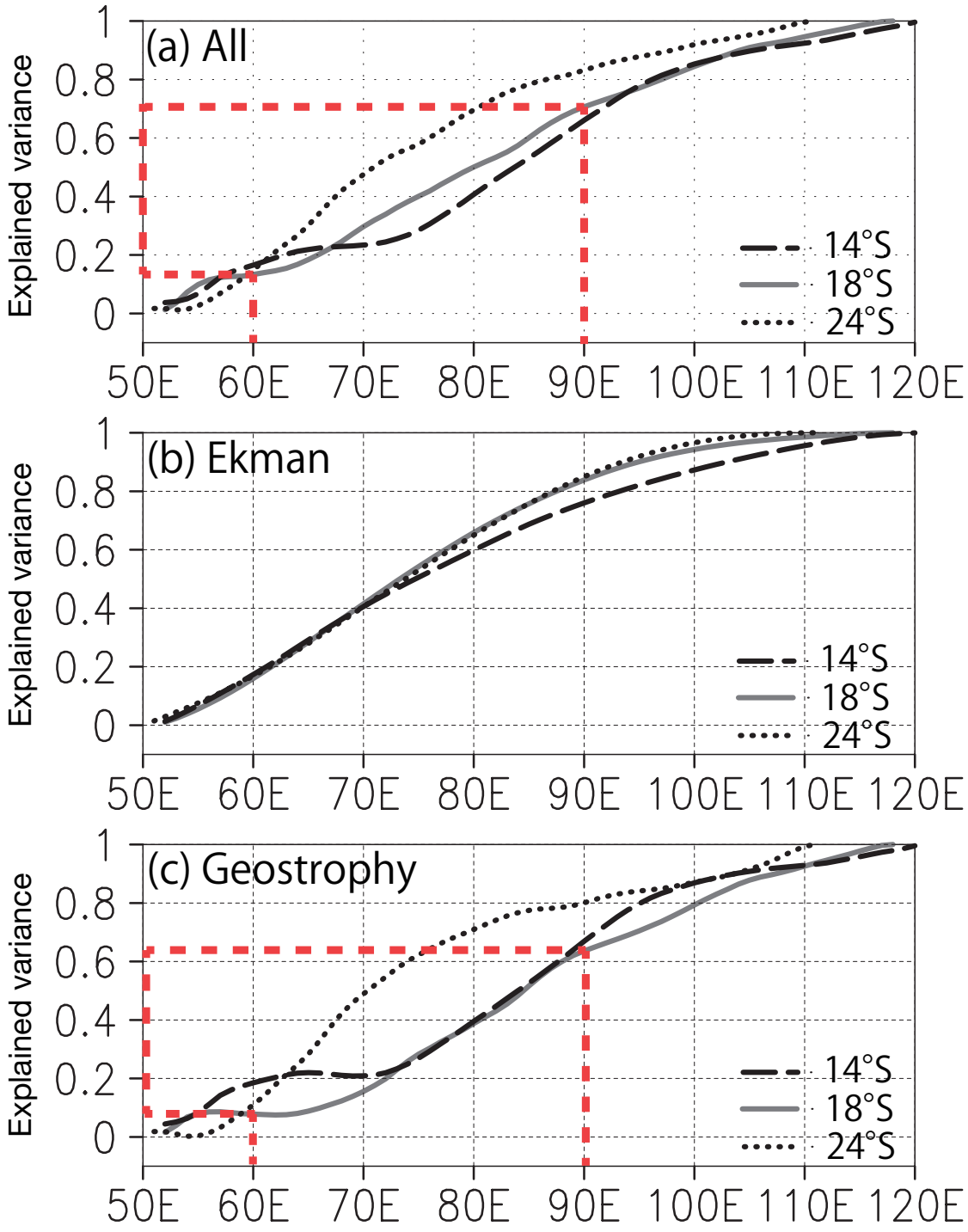

Figure 3.13: Explained variance of (a) interannual anomaly of T_{in} at 18°S (solid line), 14°S (long dashed line), and 24°S (short dashed line). (b) As in (a), but for the Ekman transport term in Eq. (4.3). (c) As in (a), but for the geostrophic transport term in Eq. (4.3).

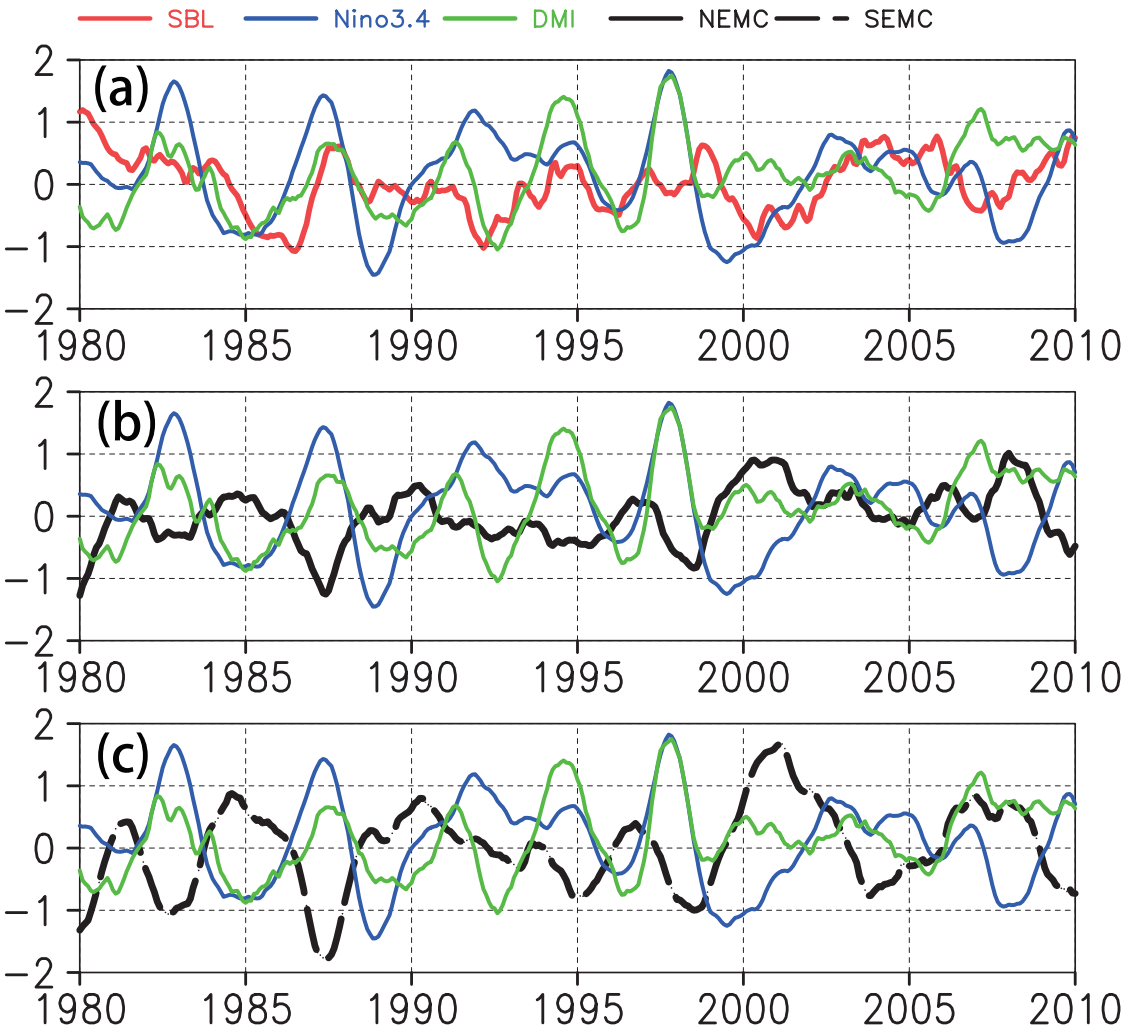

Figure 3.14: Normalized low-passed time series of (a) the SBL anomaly (red), the Niño 3.4 index (blue), and the DMI (green). (b) As in (a), but for the Niño 3.4 index (blue), the DMI (green), and the NEMC transport anomaly at 14°S (black solid). (c) As in (a), but for the Niño 3.4 index (blue), the DMI (green), the SEMC transport anomaly at 24°S (black dashed).

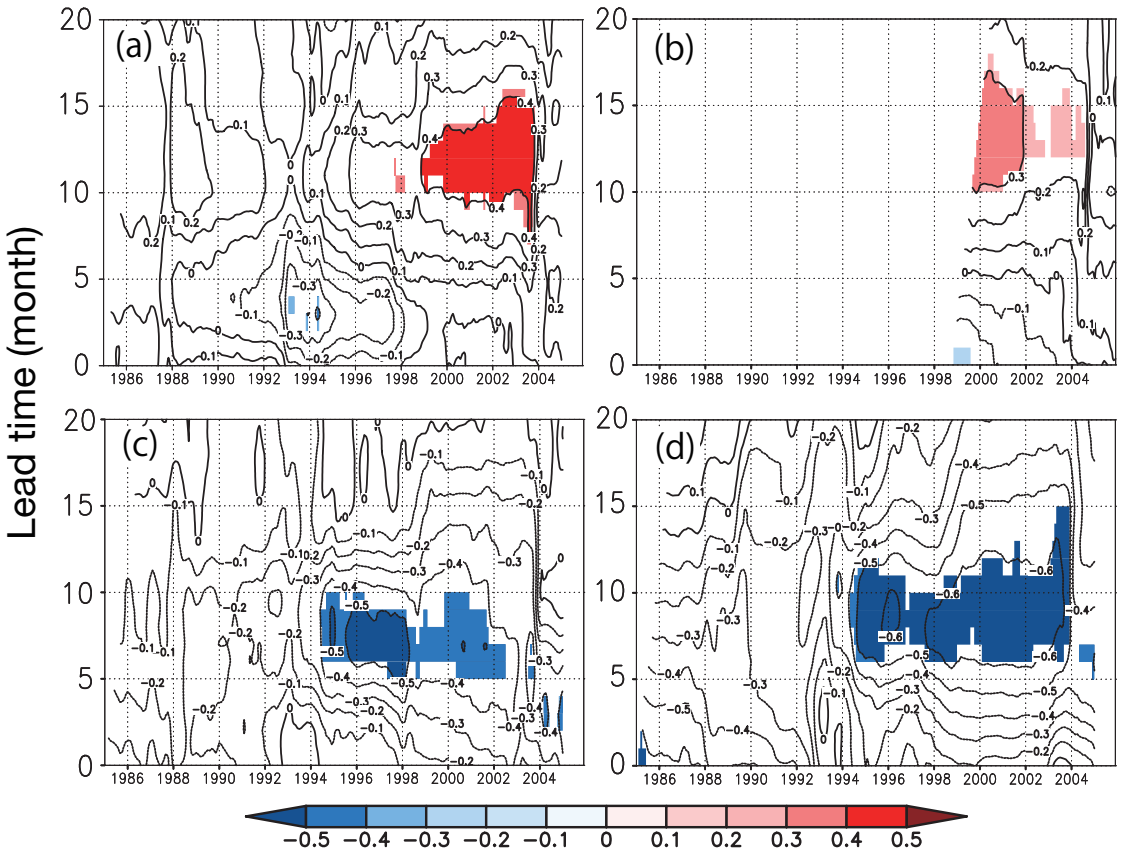

Figure 3.15: 10-year runnig lag-correlation of the Niño 3.4 index with the SBL anomaly from (a) the ORAS4 and (b) the AVISO geostrophy, (c) the NEMC transport anomaly, and (d) the SEMC transport anomaly. Correlations significant at the 90% confidence level by a two-tailed t-test are shaded. The vertical axis indicates the lead time (month) of the Niño 3.4 index, and the horizontal axis indicates the center month of each 10-year.

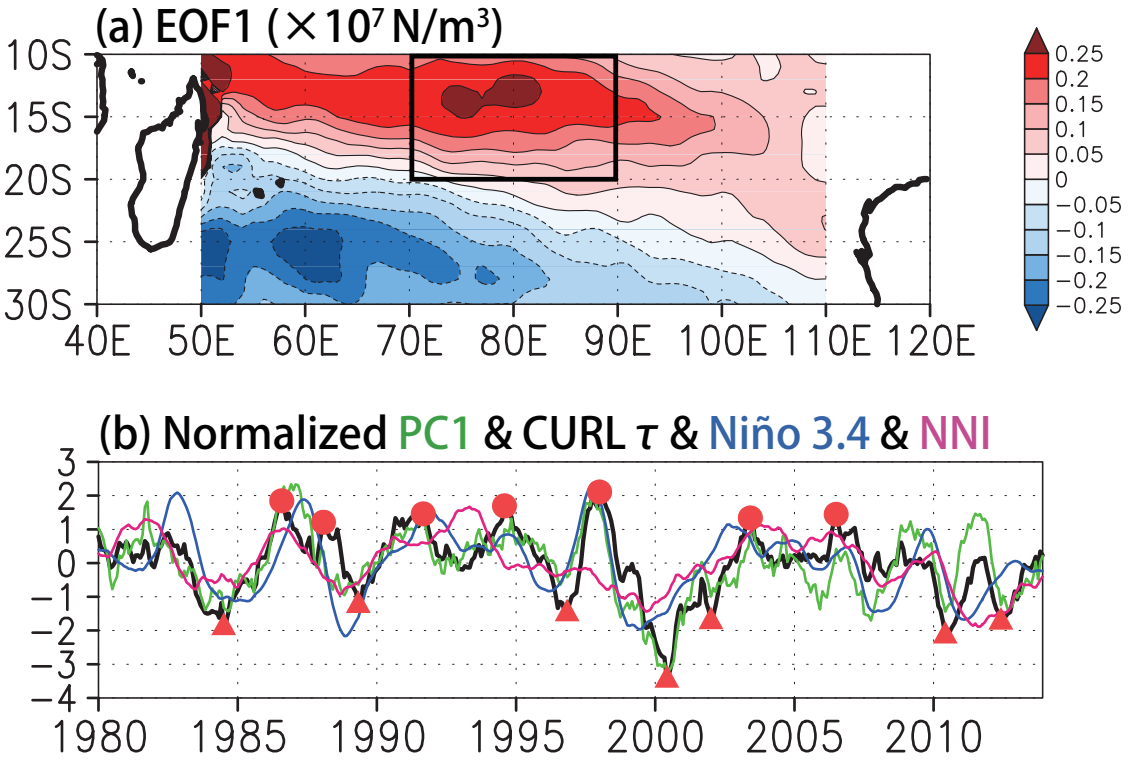

Figure 3.16: (a) Spatial pattern of the first EOF mode of wind stress curl anomalies (in 10^{-7} N/m^3). The rectangular box denotes the maximum region of wind stress curl anomalies. (b) Normalized time series of wind stress curl anomalies averaged over the black box in (a) ($curl\tau$, black), the first EOF mode (PC1, green), the Niño 3.4 index (blue), and the Ningaloo Niño index (which is defined as SST anomalies over 108°E-coast, 28°S-22°S) times -1 (NNI; magenta). All time series are smoothed using a 15-month running mean. The red closed circles (triangles) indicate maxima (minima) of the time series of $curl\tau$.

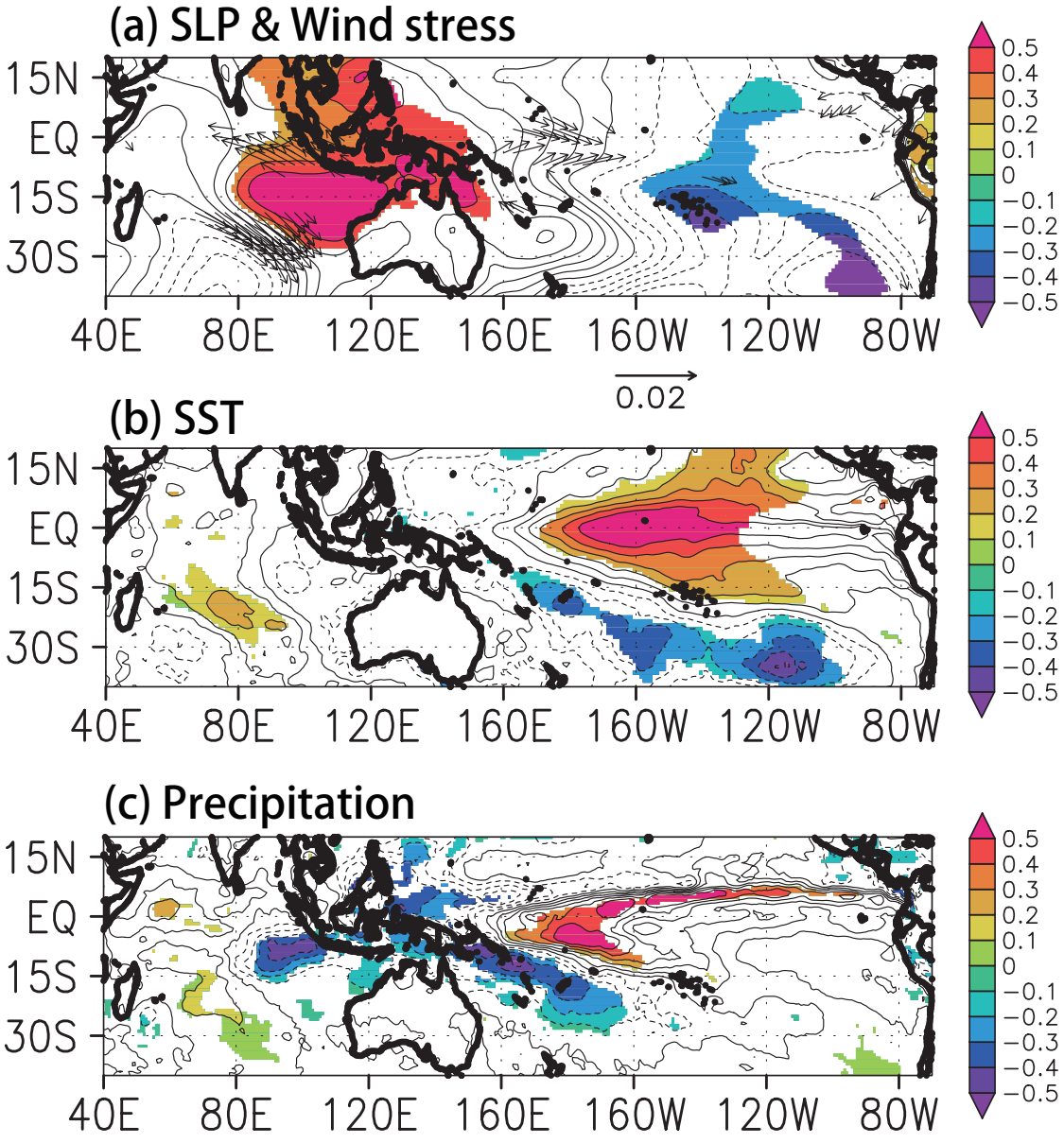

Figure 3.17: (a) Composites of SLP (in hPa, contour) and wind stress (in N/m^2, vector) anomalies for the maxima of the $curl\tau$ time series shown in Fig. 3.16b. The contour interval is 0.1 hPa. SLP (wind stress) anomalies exceeding the 90% confidence level by a two-tailed t-test are shaded (drawn). (b), (c) As in (a), but for SST (°C) and convective precipitation ($\times 10^{-3}$ m/day) anomalies, respectively. The contour interval is 0.1 °C and 0.1×10^{-3} m/day, respectively. Each composite is calculated after each data is smoothed using a 15-month running mean.

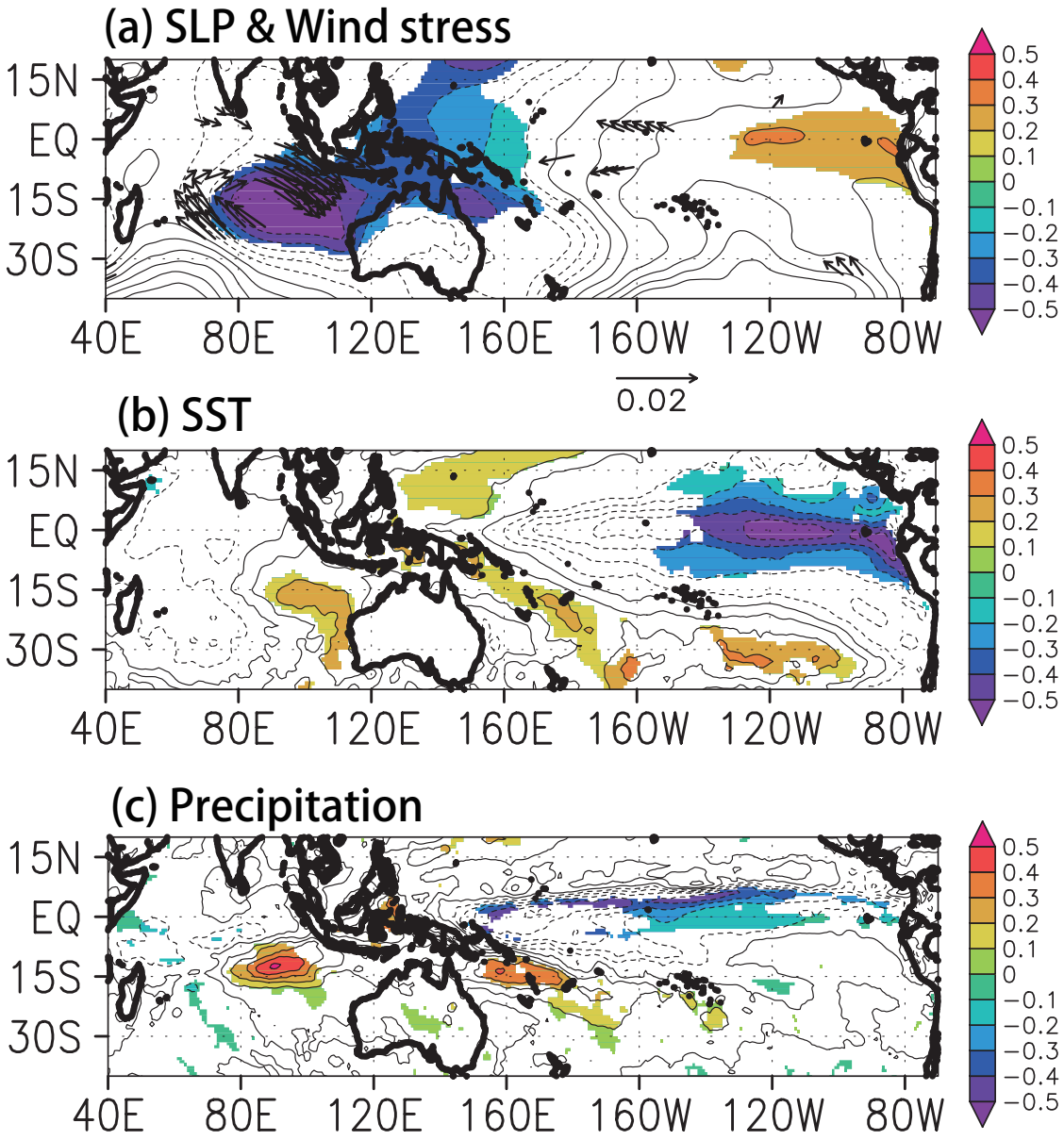

Figure 3.18: As in Fig. 3.17, but for the minima of the $curl\tau$ time series shown in Fig. 3.16b.

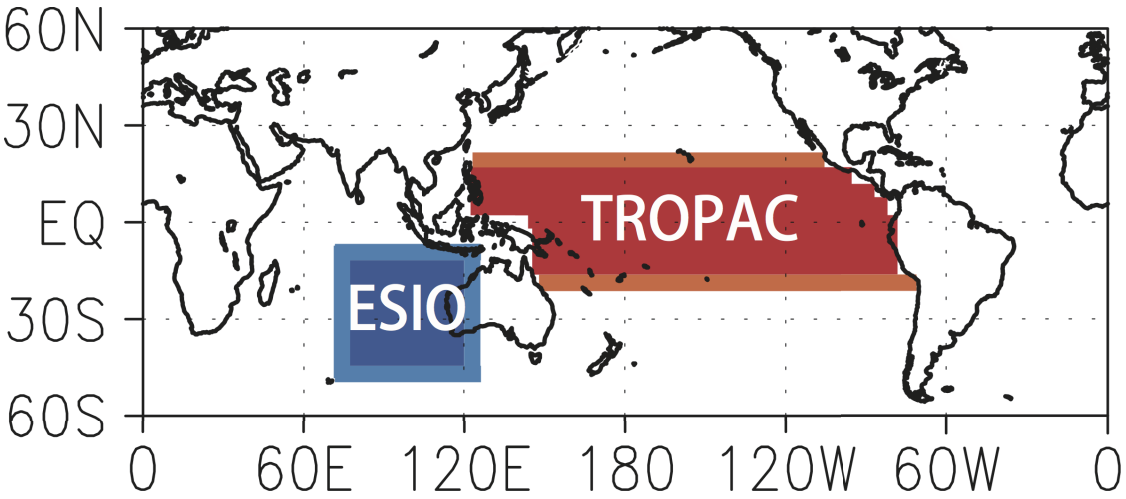

Figure 3.19: Areas where interannual SST variation is allowed in the TROPAC (red) and ESIO (blue) experiments. In the light blue and red shading area, the imposed SST anomalies are linearly decreased to zero. Modified from Fig. 1 of Tozuka et al. (2014a).

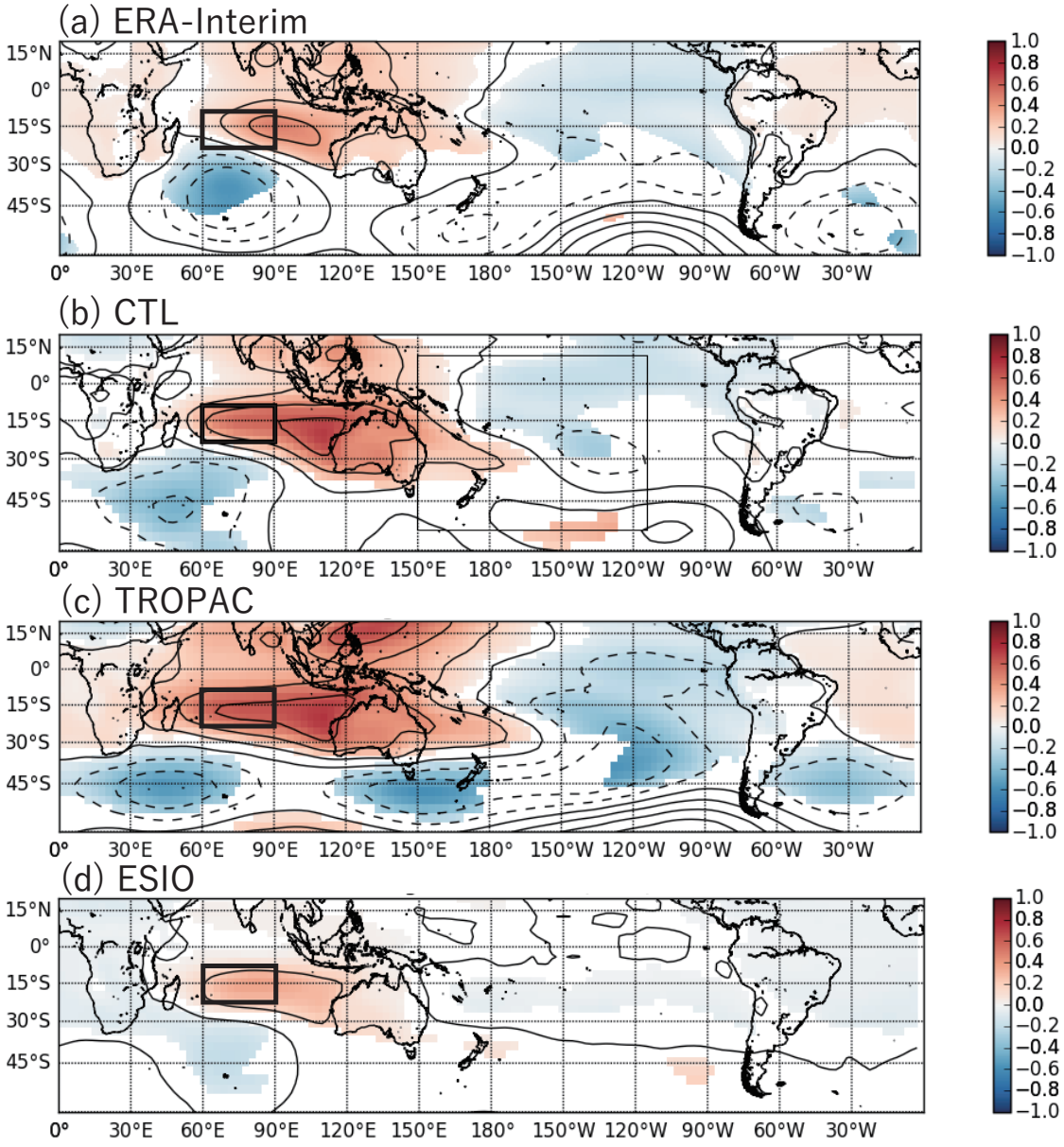

Figure 3.20: Regression coefficients of SLP anomalies [hPa] to the area-averaged wind stress curl anomaly in (a) ERA-Interim, (b) CTL, (c) TROPAC, and (d) ESIO. The black box in each panel ($60 - 90$°E, $10 - 20$°S) shows the area in which area-averaged wind stress curl is calculated. Contour intervals are 0.2 hPa and anomalies significant at the 90% confidence level by two-tailed t-test are shaded.

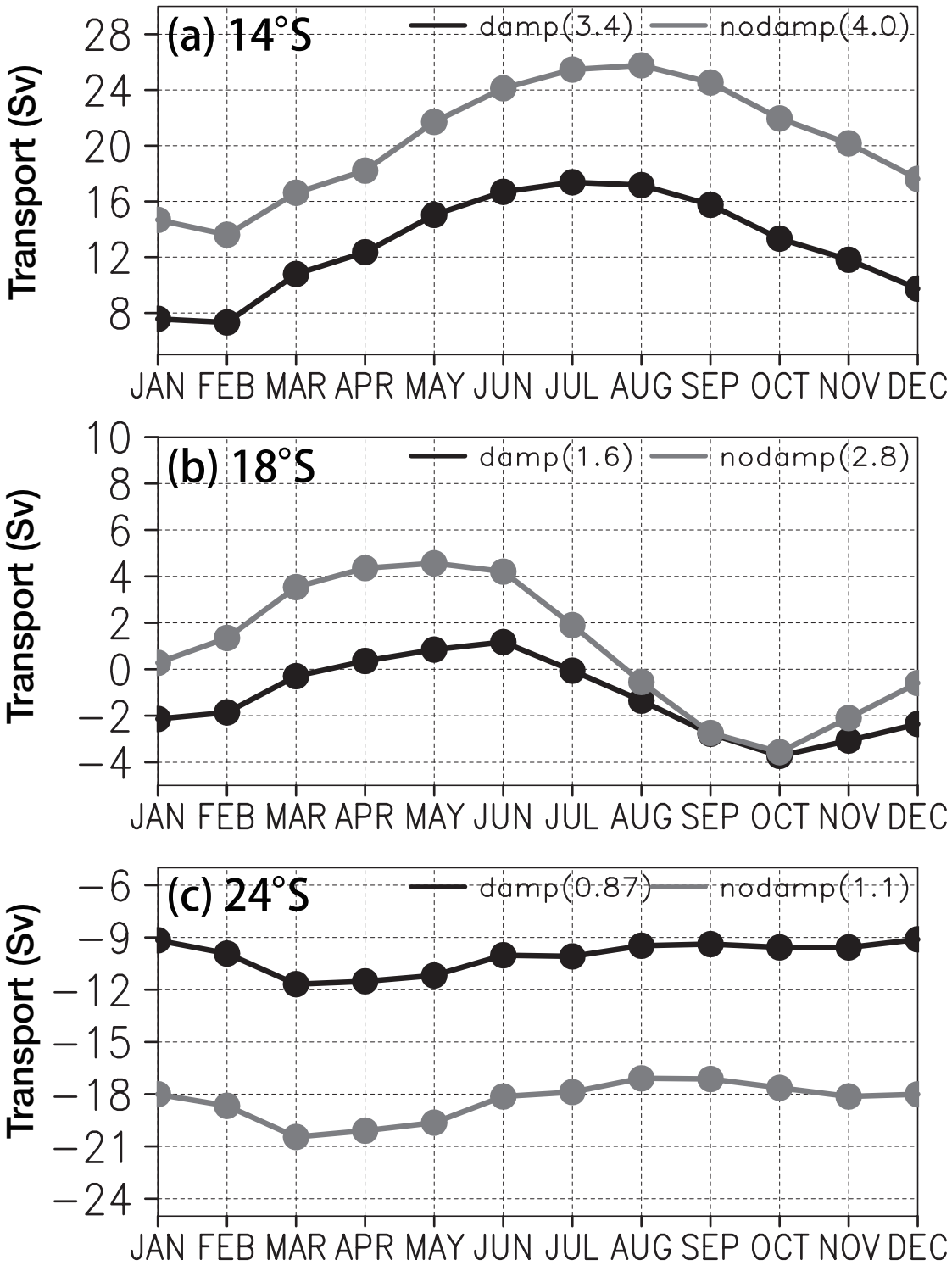

Figure 3.21: Annual march of T_{bc} at (a) $14°$S, (b) $18°$S, and (c) $24°$S obtained from the TDIR with (black line) and without (gray line) the damping term. The value in the bracket indicates the standard deviation.

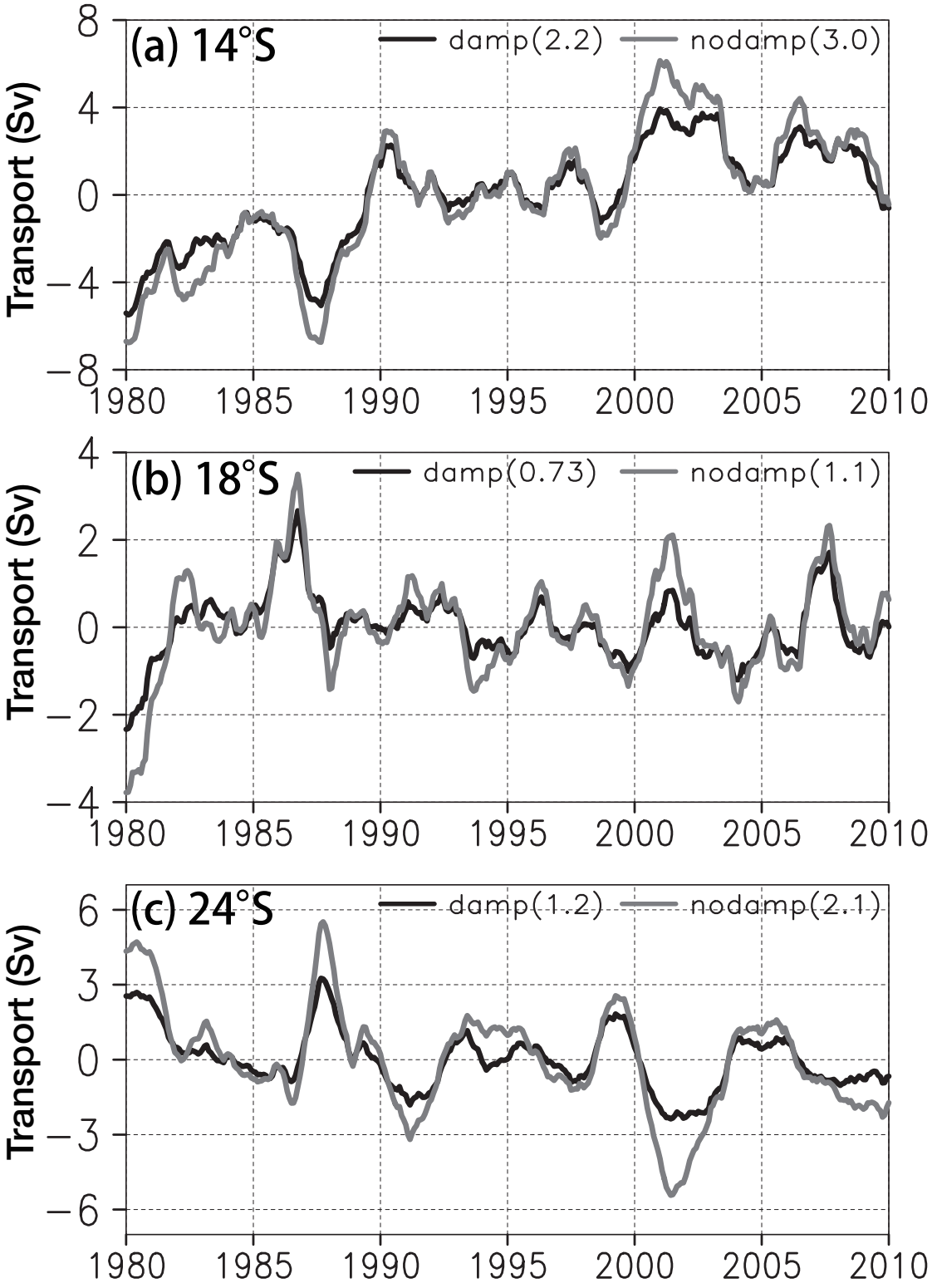

Figure 3.22: As in Fig. 3.21, but for interannual anomalies of T_{bc}.

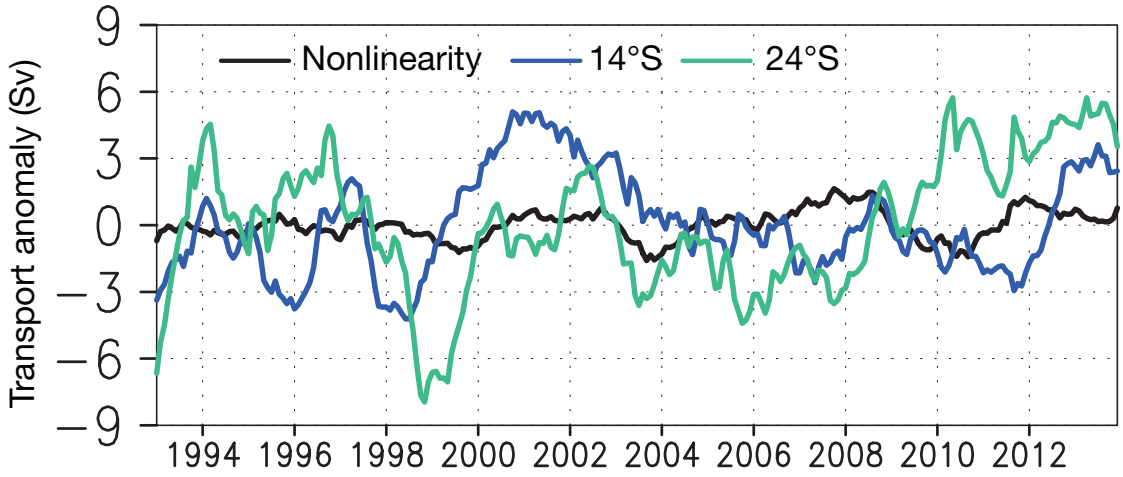

Figure 3.23: Interannual anomalies of the nonlinear term in the TDIR (black), and the meridional transports at $14°$S (blue) and $24°$S (green) within the western boundary layer. All time series are calculated from the AVISO geostrophy.

Chapter 4

General conclusions

In this thesis, the mechanism of interannual variability of the western boundary currents in the southern Indian Ocean, particularly that of the Natal Pulse and Northeast/Southeast Madagascar Current (NEMC/SEMC) is examined. This chapter summarizes the main results of this thesis (Fig. 4.1) and discusses possible impacts of this thesis and future directions.

4.1 Summary

In chapter 2, we have first investigated the generation mechanism of the Natal Pulse using observational data and high-resolution ocean general circulation model (OGCM) outputs. Since the Natal Pulse is detected by a cyclonic anomaly in the coastal region, the Natal Pulse index (NPI) is defined as an area-averaged sea surface height (SSH) anomalies and we define the Natal Pulse events as the negative peaks of the NPI exceeding -2 standard deviations. Lag composites of absolute dynamic topography (ADT), velocity, and eddy kinetic energy (EKE) anomalies show that more than 80% of the Natal Pulse events are triggered by anticyclonic eddies, which is also supported by eddy tracking results. These anticyclonic eddies propagate along the Natal Bight from around 27°S, and start to interact with mean horizontal shear of the Agulhas Current. The meander gradually develops mainly due to the barotropic conversion along the core of the Agulhas Current and the spatial pattern is determined by superposition of the barotropic conversion and advection of EKE by the eddy and/or the Agulhas Current itself. We also find that there is no bottom trapped eddy as seen in the Kuroshio large meander during the developing phase of the Natal Pulse. In addition, the amplitude of the anticyclonic eddy is one of the necessary conditions for the growth of the Natal Pulse. The sources of these anticyclonic eddies are investigated and eddy tracking results reveal that more than half of anticyclonic eddies come from the SEMC region. Furthermore, interannual variability of the Natal Pulse is examined. A statistical regression model shows that eddies from the SEMC region play a critical role in the interannual variation of the Natal Pulse, while eddies from other regions

play a minor role. As mentioned in previous studies, generation of eddies in the SEMC region are mainly explained by the barotropic conversion associated with the horizontal shear of the SEMC. Therefore, the interannual variation of the SEMC is suggested to be one of the main drivers of the interannual variations in the Natal Pulse.

In chapter 3, we have examined the dynamics of interannual variability of the NEMC and SEMC, and the relationship between these currents and basin-scale wind anomalies associated with climate modes. Analyses of observational and reanalysis data show that interannual anomalies of the NEMC/SEMC transport are more closely linked with those of the South Equatorial Current (SEC) than those of the SEC bifurcation latitude (SBL). To understand the dynamical mechanisms, interannual variations in the NEMC and SEMC transports are examined by the Time-dependent Island Rule (TDIR). The TDIR successfully reproduces their interannual variations, although slight differences in the phase and amplitude may be due to uncertainty in the phase speed of oceanic baroclinic Rossby wave, the eastern boundary conditions, and nonlinearity associated with eddy shedding. The TDIR reveals that the meridional transport anomaly in the interior region plays the key role in the interannual variations of the SBL, NEMC, and SEMC. Explained variances of the meridional transport anomaly indicates the importance of the geostrophic transport and wind stress curl anomaly around $60°$E-$90°$E. The mechanism of the wind stress curl anomaly is also discussed in relation with the ENSO, since the interannual variations of the SBL and the NEMC/SEMC transports are significantly correlated with the Niño 3.4 index with a lag of 5-15 months. Since it is suggested that diabatic heating anomalies associated with the ENSO generate wind stress curl anomalies over the central region of the southern Indian Ocean, we have conducted atmospheric general circulation model experiments that highlight the role of SST anomalies in the tropical Pacific and the southeastern Indian Ocean. These sensitivity experiments show that a Matsuno-Gill response to the Pacific SST anomalies contributes the most to the wind stress curl anomalies, while local SST anomalies in the southeastern Indian Ocean can generate about 50% of the wind stress curl anomalies. Therefore, wind stress curl

anomalies in the interior are mainly due to the ENSO and partly modified by the local air-sea interaction process in the southeastern Indian Ocean.

We note that the above mechanisms do not completely explain interannual variations in the Natal Pulse, although the ENSO is referred to as an ultimate driver of the Natal Pulse. Since the ENSO explains at most 50% of interannual variations in the SEMC ($r < 0.7$; Fig. 3.15d) and 50% of anticyclonic eddies arriving at the north of the Natal Bight come from the SEMC region, the maximum explained variance of the Natal Pulse by the ENSO is only 25%[1]. This implies that generation and interannual variations of the Natal Pulse can also be explained by probabilistic aspects associated with the generation and interactions of meso-scale eddies. For example, anticyclonic eddies in the SEMC region can grow stochastically like solitary meso-scale eddies generated by the baroclinic instability in the ocean interior. Furthermore, eddies in the SEMC may be triggered by eddies propagating along the South Indian Ocean Countercurrent (Palastanga et al. 2007; Ponsoni et al. 2016). Also, the eddy-tracking method in this study may sometimes fail to track eddies owing to sampling errors of the satellite data etc. and the exact percentages of eddies arriving at the north of the Natal Bight from the Mozambique Channel and the SEMC region are sensitive to the parameters and criteria, although the qualitative results remain the same.

In summary, this thesis has shown dynamically for the first time that interannual variations of the western boundary currents along the Madagascar coast are linked with the ENSO via atmospheric and oceanic teleconnections, and control that of the Natal Pulse to some extent (Fig. 4.1). These results suggest a new framework for interannual variations of the Indian Ocean circulation, i.e. climate variation is a driver of the mesoscale activity in the southwestern Indian Ocean.

[1]This percentage is a rough estimate based on a simple correlation analysis. For nonlinear processes examined in this study, future studies adopting more sophisticated statistical approaches are awaited.

4.2 Impacts of this thesis and future directions

This study is originally motivated by possible impacts of interannual variations of the trade winds to the Agulhas Current and Leakage. Therefore, investigation of the dynamical linkage between the Natal Pulse and Agulhas Leakage is the next step. One possible approach is multi-member ensemble simulations by a high-resolution OGCM. Nonaka et al. (2016) examined predictability of the Kuroshio Extension region and suggested that multi-member ensemble simulation is useful to understand variability of the western boundary currents. Therefore, we believe that multi-member ensemble simulation with different strength of the trade winds in the southern Indian Ocean associated with the ENSO is valuable to understand how deterministic the Natal Pulse and Agulhas Leakage are. This thesis and the proposed future works are expected to contribute to understanding of scale interaction between the global thermohaline circulation and mesoscale eddies and thus how fundamental mesoscale eddies are to global circulation.

The modeling of the southwestern Indian Ocean is quite challenging. Although the Mozambique Channel is a pathway of low-frequency variability from the tropical southern Indian Ocean to the Agulhas Leakage (Putrasahan et al. 2016) and anticyclonic eddies from the Mozambique Channel play some role in the interannual variations of the Natal Pulse, no OGCM succeeded in realistically simulating frequency and variability of the circulation in the Mozambique Channel (van der Werf et al. 2010). Also, the longitude of the retroflection of the Agulhas Current poses another challenge for numerical simulation; the retroflection positions were too west (by about 5°) in several state-of-the-art OGCMs (Loveday et al. 2014). Therefore, further effort is necessary for more realistic eddy-resolving simulation of the Natal Pulse and other mesoscale variability in the Agulhas system to improve understanding and prediction of this key region in the global climate system.

This thesis can also contribute to understanding and predictability of the air-sea interaction in the Agulhas Current, Agulhas Retroflection region, and Agulhas Return Current.

For example, the SST front in the Agulhas Return Current region is known to anchor the storm track (Ogawa et al. 2012), and maintained by oceanic processes (Ohishi et al. 2017). Since changes in SST gradient can influence the strength of the Mascarene high (Morioka et al. 2015), the present results suggest a possibility of a coherent air-sea coupled system over the whole southern Indian Ocean. It is possible that disturbances associated with the Natal Pulse or mesoscale eddies from Madagascar influence the downstream region nonlinearly, and consequently, the air-sea interaction in the Agulhas Return Current region. Therefore, it will be interesting to examine the relationship between mesoscale variability relevant to the Natal Pulse and the air-sea interaction process in the downstream region.

This study may also contribute to understanding of oceanic and climate variability in the western Indian Ocean. For example, SST anomalies off the Tanzania shelf region are affected by variability in the NEMC (Manyilizu et al. 2014). Further north, Izumo et al. (2008) showed that the SST off the Somalia coast modulates moisture supply from the ocean to the atmosphere and influences precipitation anomalies over western India associated with the Indian summer monsoon. It is possible that SST anomalies off the Tanzania shelf and Somalia is caused by anomalous heat transport by the NEMC, and results from the present study may shed new light on understanding and predicting anomalous oceanic variability and monsoon precipitation.

Results from this study may also be useful for ecosystem and fishery. For instance, the spawning area of four eel species is located to the east of Madagascar. Pous et al. (2010) suggested that the ocean circulation in the study area of the present thesis is crucial for the migration pathways of larvae. In the North Pacific, Kim et al. (2007) showed that the interannual variations of the North Equatorial Current bifurcation latitude influence the transport of Japanese eel larvae. It is possible that interannual variations of the SBL influence the life cycle of eels in the southwestern Indian Ocean.

Figures

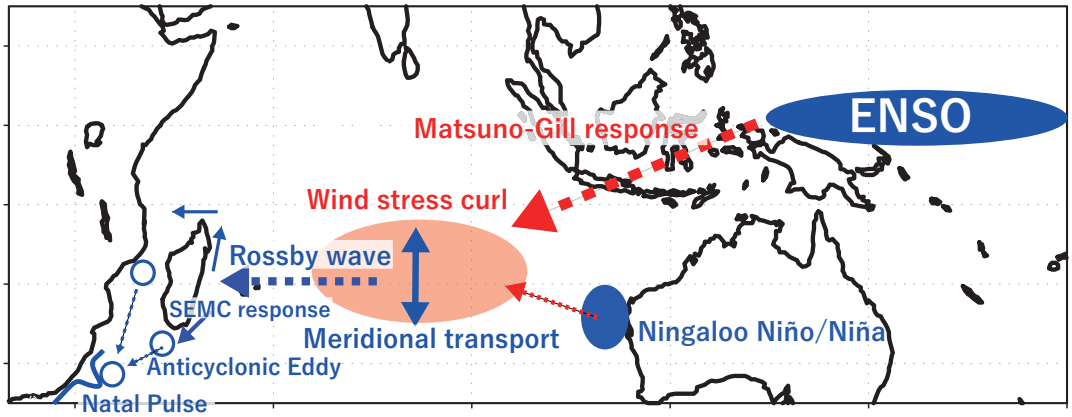

Figure 4.1: Schematic figure of the summary of this thesis. Atmospheric processes are shown in red, and oceanic ones in blue.

Appendix A

Derivation of the Time-dependent Island Rule

Following Firing et al. (1999) and Chen et al. (2014), we derive the TDIR here. The basic equations for a 1.5-layer reduced gravity model are

$$\frac{\partial u}{\partial t} + (\boldsymbol{u} \cdot \nabla)u - fv = -g' h_x + \frac{\tau^x}{\rho_0 H} + Diss(u) \tag{A.1}$$

$$\frac{\partial v}{\partial t} + (\boldsymbol{u} \cdot \nabla)v + fu = -g' h_y + \frac{\tau^y}{\rho_0 H} + Diss(v) \tag{A.2}$$

$$h_t + H\nabla \cdot \boldsymbol{u} = 0. \tag{A.3}$$

Here, (u, v) are zonal and meridional current, (τ^x, τ^y) are zonal and meridional wind stress, h is the upper layer thickness, ρ_0 is the reference density of the seawater, $H(= 290\ m)$ is the mean upper layer thickness, $g'(= 0.029\ ms^{-2})$ is the reduced gravity, and f is the Coriolis parameter. The long wave approximation and an instantaneous adjustment of coastal Kelvin waves are assumed, so that $\partial \boldsymbol{u}/\partial t$ is removed from the momentum equations. $Diss(u)$ and $Diss(v)$ represent the interfacial friction and lateral friction terms in each momentum equation, which can be ignored in the interior ocean.

Taking the cross differentiation of Eqs. (A.1) and (A.2), and substituting Eq. (A.3)

leads to the following equation for the interior ocean:

$$h_t + C_R h_x = B(x, y, t) - \epsilon h. \tag{A.4}$$

Here, $C_R(= -\beta g' H/f^2)$ is the phase speed of the first barocinic long Rossby waves, β is the meridional gradient of f, $B(x, y, t) = -\nabla \times (\boldsymbol{\tau}/\rho_0 f)$, and $\epsilon(= 2\ year^{-1})$ is the Newtonian dissipation coefficient, which was neglected in the previous studies. Integrating Eq. (A.4) along the characteristic line $(x - tC_R = const.)$ from the eastern boundary (x_e), we obtain

$$\begin{aligned} h(x, y, t) &= \frac{1}{C_R}\int_{x_e}^{x} B(x', y, t - \frac{x - x'}{C_R}) \exp[\frac{\epsilon}{C_R}(x' - x)]dx' \\ &\quad + h(x_e, y, t - \frac{x - x_e}{C_R}) \exp[\frac{\epsilon}{C_R}(x' - x)]. \end{aligned} \tag{A.5}$$

The first term on the right hand side of Eq. (A.5) indicates the baroclinic response to wind stress curl in the interior, and the second term represents effects of the Rossby waves generated by the eastern boundary forcing.

The total volume flux within the interior (T_{in}) is

$$T_{in}(y, t) = \int_{x_{w+}(y)}^{x_e(y)} H v dx'. \tag{A.6}$$

Substituting Eq. (A.1) into Eq. (A.6), we obtain

$$\begin{aligned} T_{in}(y, t) &= \int_{x_e}^{x_{w+}} \frac{\tau^x}{f\rho_0} dx' \\ &- \frac{g'H}{C_R f}\int_{x_e}^{x_{w+}} B(x', y, t - \frac{x - x'}{C_R}) \exp[\frac{\epsilon}{C_R}(x' - x_{w+})]dx' \\ &+ \frac{g'H}{f}\{h(x_e, y, t) - h(x_e, y, t - \frac{x_{w+} - x_e}{C_R})\} \exp[\frac{\epsilon}{C_R}(x_e - x_{w+})] \end{aligned} \tag{A.7}$$

The meridional transport within the western boundary layer (T_{bc}) is defined by

$$T_{bc}(y,t) = \int_{x_w(y)}^{x_{w+}(y)} Hv dx'. \tag{A.8}$$

Considering the volume conservation within the western boundary layer, we obtain

$$\int_S (h_t + H\nabla \cdot \boldsymbol{u}) dS = 0, \tag{A.9}$$

where S indicates the area enclosed by A'A"B"C"C'B' (Fig. 3.7a). Since the western boundary layer is narrow enough so that the changes in the upper layer thickness can be neglected, using the Stokes' theorem, Eq. (A.9) is reduced to

$$\oint_{C_1} H(\boldsymbol{k} \times \boldsymbol{u}) \cdot d\boldsymbol{I} = 0.$$

Here, C_1 is the path A'A" DC"C'B'(Fig. 3.7a). Therefore,

$$T_{bc}(y_n,t) - T_{bc}(y_s,t) + \int_{w_+} H(\boldsymbol{k} \times \boldsymbol{u}) \cdot d\boldsymbol{I} = 0. \tag{A.10}$$

Then, considering the vorticity equation integrated over the western boundary layer and the island, we obtain

$$\oint_{C_1} f(\boldsymbol{k} \times \boldsymbol{u}) \cdot d\boldsymbol{I} = \oint_{C_1} \frac{\boldsymbol{\tau}(t) \cdot d\boldsymbol{I}}{\rho_0 H} - \oint_{C_1} \frac{\partial}{\partial t}\boldsymbol{u} \cdot d\boldsymbol{I} - \oint_{C_1} (\boldsymbol{u} \cdot \nabla)\boldsymbol{u} \cdot d\boldsymbol{I} + \oint_{C_1} Diss(\boldsymbol{u}) \cdot d\boldsymbol{I}.$$

Because the dissipation plays a role when the island is zonally elongated (Pedlosky et al. 1997), ignoring the time-dependent and dissipation terms leads to

$$\oint_{C_1} f(\boldsymbol{k} \times \boldsymbol{u}) \cdot d\boldsymbol{I} = \oint_{C_1} \frac{\boldsymbol{\tau}(t) \cdot d\boldsymbol{I}}{\rho_0 H} - \oint_{C_1} (\boldsymbol{u} \cdot \nabla)\boldsymbol{u} \cdot d\boldsymbol{I}. \tag{A.11}$$

Substituting Eq. (A.11) into Eq. (A.10) and using the β-plane approximation ($f =$

$f_s + \beta(y - y_s)$), we obtain

$$\begin{aligned} y_n T_{bc}(y_n, t) - y_s T_{bc}(y_s, t) &+ \int_{C_{w+}} yH(\boldsymbol{k} \times \boldsymbol{u}) \cdot d\boldsymbol{I} \\ &= \oint_{C_1} \frac{\boldsymbol{\tau}(t) \cdot d\boldsymbol{I}}{\rho_0 \beta} - \frac{H}{\beta} \oint_{C_1} (\boldsymbol{u} \cdot \nabla)\boldsymbol{u} \cdot d\boldsymbol{I}. \end{aligned} \quad \text{(A.12)}$$

Here, C_{w+} is the path C'B'A (Fig. 3.7a). From Eqs. (A.10) and (A.12), we can eliminate $T_{bc}(y_s, t)$ and obtain

$$\begin{aligned} T_{bc}(y_n, t) &= \frac{1}{\Delta y} \oint_{C_1} \frac{\boldsymbol{\tau}(t) \cdot d\boldsymbol{I}}{\rho_0 \beta} \\ &- \frac{1}{\Delta y} \int_{C_{w+}} (y - y_s) H(\boldsymbol{k} \times \boldsymbol{u}) \cdot d\boldsymbol{I} - \frac{H}{\beta \Delta y} \oint_{C_1} (\boldsymbol{u} \cdot \nabla)\boldsymbol{u} \cdot d\boldsymbol{I}, \end{aligned} \quad \text{(A.13)}$$

where $\Delta y = y_n - y_s$. Equation (A.13) is the essence of the TDIR (Firing et al. 1999) and indicates that $T_{bc}(y_n, t)$ balances with the transport driven by the local wind stress and the transport from the ocean interior, which are flowing northward with the ratio of $(y - y_s)/(y_n - y_s)$.

Next, we rewrite the second term on the right hand side of Eq. (A.13). Integrating Eq. (A.3) from x_{w+} to x_e gives

$$\begin{aligned} \int_{x_{w+}}^{x_e} h_t dx &= \int_{x_{w+}}^{x_e} (-Hu_x - Hv_y) dx \\ &= -H \int_{x_{w+}}^{x_e} \frac{\partial u}{\partial x} dx - H \int_{x_{w+}}^{x_e} \frac{\partial v}{\partial y} dx \\ &= -Hu(x_e) + Hu(x_{w+}) \\ &\quad -\frac{\partial}{\partial y} T_{in}(y, t) + Hv(x_e) \frac{dx_e}{dy} - Hv(x_{w+}) \frac{dx_{w+}}{dy}. \end{aligned} \quad \text{(A.14)}$$

Here, we have used the Leibniz rule, i.e.

$$\frac{\partial}{\partial y}\int_{x_{w+}}^{x_e} v dx = \int_{x_{w+}}^{x_e} \frac{\partial v}{\partial y} dx + v(x_e)\frac{dx_e}{dy} - v(x_{w+})\frac{dx_{w+}}{dy}.$$

Taking $\int_{y_s}^{y_n}(y_n - y_s) \times (A.14)\, dy$ and substituting Eq. (A.13), we obtain

$$\begin{aligned} T_{bc}(y_n,t) = & - T_{in}(y_n,t) + \frac{1}{\Delta y}\int_{y_s}^{y_n} T_{in}(y,t)dy \\ & + \frac{1}{\Delta y}\oint_{C_1} \frac{\boldsymbol{\tau}(t)\cdot d\boldsymbol{I}}{\rho_0 \beta} \\ & - \frac{1}{\Delta y}\int_{y_s}^{y_n}\int_{x_{w+}}^{x_e}(y-y_s)\frac{\partial h}{\partial t}dxdy \\ & - \frac{1}{\Delta y}\int_{CBA}(y-y_s)H(\boldsymbol{k}\times\boldsymbol{u})\cdot d\boldsymbol{I} \\ & - \frac{H}{\beta\Delta y}\oint_{C_1}(\boldsymbol{u}\cdot\nabla)\boldsymbol{u}\cdot d\boldsymbol{I}. \end{aligned} \tag{A.15}$$

Equation (A.15) indicates that $T_{bc}(y_n,t)$ balances with the meridional transport in the interior, the meridionally averaged interior transport, the circulation generated by wind stress around the island, the meridionally averaged upper layer thickness variation (this term is referred as the storage term associated with upper layer thickness anomaly), the inflow from the eastern boundary, and the vorticity flux associated with eddy shedding (Pedlosky et al. 1997) (Fig. 3.7c). The inflow from the eastern boundary is included to incorporate the effect of the Indonesian Throughflow. To obtain $T_{bc}(y,t)$, we consider the volume conservation from y to y_n (Fig. 3.7b). Integrating Eq. (A.3) over this area, we obtain

$$\begin{aligned} T_{bc}(y,t) = & -T_{in}(y,t) + \int_{y}^{y_n}\int_{x_{w+}}^{x_e}\frac{\partial h}{\partial t}dxdy \\ & + T_{in}(y_n,t) + T_{bc}(y_n,t) \\ & + \int_{BA} H(\boldsymbol{k}\times\boldsymbol{u})\cdot d\boldsymbol{I}. \end{aligned} \tag{A.16}$$

Then, substituting Eq. (A.15) into the terms in the second line of Eq. (A.16) yields

$$
\begin{aligned}
T_{bc}(y,t) = \; & - \; T_{in}(y,t) + \frac{1}{\Delta y}\int_{y_s}^{y_n} T_{in}(y,t)dy \\
& + \; \frac{1}{\Delta y}\oint_{C_1} \frac{\boldsymbol{\tau}(t)\cdot d\boldsymbol{I}}{\rho_0 \beta} \\
& + \; \int_{y}^{y_n}\int_{x_{w+}}^{x_e} \frac{\partial h}{\partial t} dxdy - \frac{1}{\Delta y}\int_{y_s}^{y_n}\int_{x_{w+}}^{x_e} (y-y_s)\frac{\partial h}{\partial t} dxdy \\
& - \; \frac{1}{\Delta y}\int_{CBA} (y-y_s) H(\boldsymbol{k}\times\boldsymbol{u})\cdot d\boldsymbol{I} + \int_{BA} H(\boldsymbol{k}\times\boldsymbol{u})\cdot d\boldsymbol{I} \\
& - \; \frac{H}{\beta\Delta y}\oint_{C_1} (\boldsymbol{u}\cdot\nabla)\boldsymbol{u}\cdot d\boldsymbol{I}. \qquad \text{(A.17)}
\end{aligned}
$$

Note that if we ignore the effect of inflow from the eastern boundary, Rossby waves generated by the eastern boundary forcing, and nonlinear effects, we can obtain Eqs. (4.1) to (4.4).

Acknowledgments

Firstly, I would like to express my sincere gratitude to my advisor Tomoki Tozuka for his sincere support of my Ph.D. studies and related research. His guidance helped me of writing this thesis, research, and shaping personality as a scientist. I could not finish my Ph.D. study without his ceaseless encouragement. I am really honored to be his student.

I would like to thank my dissertation committee members, Hiroyasu Hasumi, Toshiyuki Hibiya, Yukio Masumoto, and Hiroaki Miura for their time and helpful comments. I am deeply grateful to Bo Qiu and Shuiming Chen for their hospitality and warm guidance during my internship at University of Hawaii at Manoa. This study has benefited from discussions with Ichiro Yasuda, Eitaro Oka, Kelvin Richards, Niklas Schneider, Nikolai Maximenko, James Potemra, and Eric Firing. I am much obliged to Takeshi Doi, Yushi Morioka, Takahito Kataoka, and Shun Ohishi for their comments and supports. They are good models for me to emulate as a graduate student and scientist.

I am also thankful to Yoshihiro Niwa, Yuki Tanaka, Pascal Oettli, Kunihiro Aoki, Taira Nagai, Takashi Ijichi, Michiya Hayashi, Yohei Onuki, Ryosuke Shibuya, Tomoaki Takagi, Tamaki Suematsu, Ayumu Miyamoto, Hajime Ishii, Chia-Rui Ong, Wei Yang, Satoru Endo, Chiho Tanizaki, Shoichiro Kido, Anne Takahashi, Katsutoshi Fukuzawa, Shuhei Matsugishi, Emiri Kobori, Marvin Seow Xiang Ce, Koichi Sugiyama, Takuya Jinno, Ryo Kobayashi, Kazumichi Murata, Kaori Sasaki, and all past and presents members of Atmoshpheric and Oceanic Science Group and faculty members of Department of Earth and Planetary Science. Also, I give a special thanks to all classmates and friends, particularly Tsubasa Kohyama, Masashi Minamide, Takafumi Kawakami, and Shunya Kono. I am

also grateful to the members of Qiu group and the staff at Universith of Hawaii at Manoa.

I would like to acknowledge the funding sources. I was supported by Research Fellowship of Japan Society for the Promotion of Science (JSPS) for Young Scientist, and Leading Graduate Course for Frontiers of Mathematical Sciences and Physics.

Last but not the least, I would like to express deepest gratitude to my father, mother, sister, grandparents, and best buddy dog. I would like to thank my family for supporting me throughout my life. I hope this thesis will reach my grandfather in heaven.

References

Arruda, W., V. Zharkov, B. Deremble, D. Nof, and E. Chassignet (2014), A New Model of Current Retroflection Applied to the Westward Protrusion of the Agulhas Current, *J. Phys. Oceanogr.*, *44*(12), 3118–3138, doi: /10.1175/JPO-D-14-0054.1.

Backeberg, B. C., P. Penven, and M. Rouault (2012), Impact of intensified Indian Ocean winds on mesoscale variability in the Agulhas system, *Nat. Clim. Change*, *2*(8), 608–612, doi: /10.1038/nclimate1587.

Backeberg, B. C., and C. J. C. Reason (2010), A connection between the South Equatorial Current north of Madagascar and Mozambique Channel eddies, *Geophys. Res. Lett.*, *37*(4), L04,604, doi:10.1029/2009GL041950.

Balmaseda, M. A., K. Mogensen, and A. T. Weaver (2013), Evaluation of the ECMWF ocean reanalysis system ORAS4, *Quart. J. Roy. Meteorol. Soc.*, *139*(674), 1132–1161.

Beal, L. M., and S. Elipot (2016), Broadening not strengthening of the Agulhas Current since the early 1990s, *Nature*, *540*(7634), 570–573, doi: /10.1038/nature19853.

Beal, L. M., S. Elipot, A. Houk, and G. M. Leber (2015), Capturing the Transport Variability of a Western Boundary Jet: Results from the Agulhas Current Time-Series Experiment (ACT)*, *J. Phys. Oceanogr.*, *45*(5), 1302–1324, doi: /10.1175/JPO-D-14-0119.1.

Beal, L. M., et al. (2011), On the role of the Agulhas system in ocean circulation and climate, *Nature*, *472*(7344), 429–436. doi: /10.1038/nature09983.

Behera, S. K., and T. Yamagata (2001), Subtropical SST dipole events in the southern Indian Ocean, *Geophys. Res. Lett.*, *28*(2), 327–330.

Beron-Vera, F. J., Y. Wang, M. J. Olascoaga, G. J. Goni,and G. Haller (2013), Objective Detection of Oceanic Eddies and the Agulhas Leakage, *J. Phys. Oceanogr.*, *43*(7), 1426–1438. doi: /10.1175/JPO-D-12-0171.1.

Biastoch, A., J. V. Durgadoo, A. K. Morrison, E. van Sebille, W. Weijer, and S. M. Griffies (2015), Atlantic multi-decadal oscillation covaries with Agulhas leakage, *Nat. Commun.*, *6*, 10082, doi: /10.1038/ncomms10082.

Biastoch, A., C. W. Böning, F. U. Schwarzkopf, and J. R. E. Lutjeharms (2009), Increase in Agulhas leakage due to poleward shift of Southern Hemisphere westerlies, *Nature*, *462*(7272), 495–498, doi: /10.1038/nature08519.

Biastoch, A., C. W. Böning, and J. R. E. Lutjeharms (2008), Agulhas leakage dynamics affects decadal variability in Atlantic overturning circulation, *Nature*, *456*(7221), 489–492, doi: /10.1038/nature07426.

Biastoch, A., and W. Krauss (1999), The Role of Mesoscale Eddies in the Source Regions of the Agulhas Current, *J. Phys. Oceanogr.*, *29*(9), 2303–2317. doi:

/10.1175/1520-0485(1999)029<2303:TROMEI>2.0.CO;2.

Braby, L., B. C. Backeberg, I. Ansorge, M. J. Roberts, M. Krug, and C. J. C. Reason, (2016), Observed eddy dissipation in the Agulhas Current, *Geophys. Res. Lett.*, *43*(15), 8143–8150. doi: /10.1002/2016GL069480.

Bryden, H. L., L. M. Beal, and L. M. Duncan (2005), Structure and transport of the Agulhas current and its temporal variability, *J Oceanogr*, *61*(3), 479–492. doi: /10.1007/s10872-005-0057-8.

Chelton, D. B., M. G. Schlax, and R. M. Samelson (2011), Global observations of nonlinear mesoscale eddies, *Prog. Oceanogr.*, *91*(2), 167–216, doi: /10.1016/j.pocean.2011.01.002.

Chelton, D. B., M. G. Schlax, and R. M. Samelson, and R. A. de Szoeke (2007), Global observations of large oceanic eddies, *Geophys. Res. Lett.*, *34*(15), 1–5, doi: /10.1029/2007GL030812.

Chen, R., A. F. Thompson, and G. R. Flierl (2016), Time-Dependent Eddy-Mean Energy Diagrams and Their Application to the Ocean, *J. Phys. Oceanogr.*, *46*(9), 2827–2850, doi: /10.1175/JPO-D-16-0012.1.

Chen, R., G. R. Flierl, and C. Wunsch (2014), A description of local and nonlocal eddy–mean flow interaction in a global eddy-permitting state estimate, *J. Phys. Oceanogr.*, 44, 2336–2352, doi:10.1175/JPO-D-14-0009.1.

Chen, Z., and L. Wu (2011), Dynamics of the seasonal variation of the North Equatorial Current bifurcation, *J. Geophys. Res.*, *116*, C02,018, doi:10.1029/2010JC006664.

Chen, Z., L. Wu, B. Qiu, S. Sun, and F. Jia (2014), Seasonal Variation of the South

Equatorial Current bifurcation off Madagascar, *J. Phys. Oceanogr.*, *44*(2), 618–631.

de Ruijter, W. P. M., H. M. van Aken, E. J. Beier, J. R. Lutjeharms, R. P. Matano, and M. W. Schouten (2004), Eddies and dipoles around South Madagascar: Formation, pathways and large-scale impact, *Deep Sea Res., Part I*, 51(3), 383–400.

de Ruijter, W. P. M., P. J. van Leeuwen, and J. R. Lutjeharms (1999), Generation and evolution of Natal Pulses: Solitary meanders in the Agulhas Current, *J. Phys. Oceanogr.*, 29(12), 3043–3055.

Dee, D., et al. (2011), The ERA-Interim reanalysis: Configuration and performance of the data assimilation system, *Quart. J. Roy. Meteorol. Soc.*, *137*(656), 553–597.

Doi, T., T. Tozuka, and T. Yamagata (2010), The Atlantic meridional mode and its coupled variability with the Guinea Dome, *J. Climate*, *23*(2), 455–475, doi: 10.1175/2009JCLI3198.1.

Durgadoo, J. V., S. Rühs, A. Biastoch, and C. W. B. Böning (2017), Indian Ocean sources of Agulhas leakage, *J. Geophys. Res.. Ocean*, *122*(4), 3481–3499. doi: /10.1002/2016JC012676.

Durgadoo, J. V., B. R. Loveday, C. J. C Reason, P. Penven, and A. Biastoch (2013), Agulhas Leakage Predominantly Responds to the Southern Hemisphere Westerlies. *J. Phys. Oceanogr.*, *43*(10), 2113–2131. doi: /10.1175/JPO-D-13-047.1.

Elipot, S., and L. M. Beal (2015), Characteristics, Energetics, and Origins of Agulhas Current Meanders and Their Limited Influence on Ring Shedding. *J. Phys.*

Oceanogr., *45*(9), 2294–2314. doi: /10.1175/JPO-D-14-0254.1.

Emanuel, K. A. (1991), A scheme for representing cumulus convection in large-scale models, *J. Atmos. Sci.*, *48*(21), 2313–2329.

Endoh, T., and T. Hibiya (2001), Numerical simulation of the transient response of the Kuroshio leading to the large meander formation south of Japan, *J. Geophys. Res.*, *106*(Cll), 26,833-26,850.

Feng, M., M. J. McPhaden, S. P. Xie, and J. Hafner (2013), La Niña forces unprecedented Leeuwin Current warming in 2011, *Sci. Rep.*, *3*(1), 1277. doi: /10.1038/srep01277.

Firing, E., B. Qiu, and W. Miao (1999), Time-dependent island rule and its application to the time-varying North Hawaiian Ridge Current, *J. Phys. Oceanogr.*, *29*(10), 2671– 2688.

Gill, A. E. (1980), Some simple solutions for heat-induced tropical circulation, *Quart. J. Roy. Meteorol. Soc.*, *106*(449), 447–462.

Gill, A. E., and E. H. Schumann (1979), Topographically Induced Changes in the Structure of an Inertial Coastal Jet: Application to the Agulhas Current. *J. Phys. Oceanogr.*. doi: /10.1175/1520-0485(1979)009<0975:TICITS>2.0.CO;2.

Gründlingh, M. L. (1979), Observation of a large meander in the Agulhas Current. *J. Geophys. Res.Oceans*, *84*, 3776–3778.

Guan, Z., S. Iizuka, M. Chiba, S. Yamane, K. Ashok, M. Honda, and T. Yamagata (2000), Frontier atmospheric general circulation model version 1.0 (FrAM1.0): model clima- tology, *Tech Rep*, pp. 1–27.

Guastella, L. A., and M. J. Roberts (2016), Dynamics and role of the Durban cyclonic eddy in the KwaZulu-Natal Bight ecosystem. *Afr. J. Mar. Sci.*, *38*, sup1, S23-S42. doi: /10.2989/1814232X.2016.1159982.

Godfrey, J. (1989), A Sverdrup model of the depth-integrated flow for the world ocean allowing for island circulations, *Geophys. Astrophys. Fluid Dyn.*, *45*(1-2), 89–112.

Halo, I., B. Backeberg, P. Penven, I. Ansorge, C. J. C. Reason, and J. E. Ullgren (2014a), Eddy properties in the Mozambique Channel: A comparison between observations and two numerical ocean circulation models, *Deep Sea Res. Part II*, *100*, 38–53. doi: /10.1016/j.dsr2.2013.10.015.

Halo, I., P. Penven, B. Backeberg, I. Ansorge, F. Shillington, and R. Roman (2014b), Mesoscale eddy variability in the southern extension of the East Madagascar Current: Seasonal cycle, energy conversion terms, and eddymean properties, *J. Geophys. Res. Oceans*, 119, 7324–7356, doi:10.1002/2014JC009820.

Harris, T. F. W., R. Legeckism, and D. van Forest (1978), Satelfite infra-red images in the Agulhas Current System. *Deep Sea Res., 25*, 543–548.

Harrison, D. E., and A. R. Robinson (1978), Energy analysis of open regions of turbulent flows - mean eddy energetics of a numerical ocean circulation experiment, *Dyn. Atmos. Oceans*, *2*(2), 185–211. doi: /10.1016/0377-0265(78)90009-X.

Hirst, A. C., and J. Godfrey (1993), The role of Indonesian Throughflow in a global ocean GCM, *J. Phys. Oceanogr.*, *23*(6), 1057–1086.

Hughes, G. R., P. Luschi, R. Mencacci, and F. Papi (1998), The 7000-km oceanic

journey of a leatherback turtle tracked by satellite, *J. Exp. Mar. Bio. Ecol.*, *229*(2), 209–217. doi: /10.1016/S0022-0981(98)00052-5.

Izumo, T., C. de Boyer Montégut, J.-J. Luo, S. K. Behera, S. Masson, and T. Yamagata (2008), The role of the western Arabian Sea upwelling in Indian monsoon rainfall variability, *J. Clim.*, 21(21), 5603–5623.

Jury, M. R., H. R. Valentine, and J. R. E. Lutjeharms (1993), Influence of the Agulhas Current on Summer Rainfall along the Southeast Coast of South Africa, *J. Appl. Meteor.*, doi: /10.1175/1520-0450(1993)032<1282:IOTACO>2.0.CO;2.

Kalnay, E., et al. (1996), The NCEP/NCAR 40-year reanalysis project, *Bull. Amer. Meteor. Soc*., *77*(3), 437-471.

Kataoka, T., T. Tozuka, S. Behera, and T. Yamagata (2014), On the Ningaloo Niño/Niña, *Clim. Dyn.*, *43*(5–6), 1463–1482. doi: /10.1007/s00382-013-1961-z.

Kawabe, M. (1995), Variations of Current Path, Variability, and Volume Transport of the Kuroshio in Relation with the Large Meander, *J. Phys. Oceanogr.*, *25*, 3103–3117.

Kim, H., S. Kimura, A. Shinoda, T. Kitagawa, Y. Sasai, and H. Sasaki (2007), Effect of El Niño on migration and larval transport of the Japanese eel (Anguilla japonica), *ICES J. Mar. Sci.*, *64*(7), 1387–1395, doi:10.1093/icesjms/fsm091.

Kurian, J., F. Colas, X. Capet, J. C. McWilliams, and D. B. Chelton (2011), Eddy properties in the California Current System, *J. Geophys. Res. Ocean*, *116*(8), 1–18. doi: /10.1029/2010JC006895.

Le Bars, D., H. A. Dijkstra, and W. P. M. de Ruijter (2013), Impact of the Indonesian

Throughflow on Agulhas leakage, *Ocean Sci.*, *9*, 773–785.

Le Bars, D., W. P. M. de Ruijter, and H. A. Dijkstra (2012), A New Regime of the Agulhas Current Retroflection: Turbulent Choking of Indian–Atlantic leakage, *J. Phys. Oceanogr.*, *42*(7), 1158–1172. doi: /10.1175/JPO-D-11-0119.1.

Leber, G. M., L. M. Beal, and S. Elipot (2016), Wind and current forcing combine to drive strong upwelling in the Agulhas Current, *J. Phys. Oceanogr.*, *47*(1), 123-134. doi: /10.1175/JPO-D-16-0079.1.

van Leeuwen, P. J., W. P. M. de Ruijter, and L. R. E. Lutjeharms (2000), Natal pulses and the formation of Agulhas rings, *J. Geophys. Res.. Oceans*, *105*(C3), 6425–6436. doi: /10.1029/1999JC900196.

Li, J., and A. J. Clarke (2004), Coastline direction, interannual flow, and the strong El Niño currents along Australia's nearly zonal southern coast, *J. Phys. Oceanogr.*, *34*(11), 2373–2381.

Loveday, B. R., J. V. Durgadoo, C. J. C. Reason, A. Biastoch, and P. Penven (2014), Decoupling of the Agulhas Leakage from the Agulhas Current, *J. Phys. Oceanogr.*, *44*(7), 1776–1797. doi: /10.1175/JPO-D-13-093.1.

Lutjeharms, J. R. E. (2006). *The Agulhas Current*. Springer, New York, 329pp.

Lutjeharms, J. R. E., O. Boebel, P. C. F. van der Vaart, W. P. M. de Ruijter, T. Rossby, and H. L. Bryden (2001), Evidence that the Natal Pulse involvs the Agulhas Current to its full depth, *Geophys. Res. Lett.*, *28*(18), 3449–3452.

Lutjeharms, J. R. E., and H. R. Roberts (1988), The Natal pulse: An extreme transient on the Agulhas Current, *J. Geophys. Res.*, *93*(C1), 631. doi:

/10.1029/JC093iC01p00631.

Lutjeharms, J. R. E. (1981), Features of the southern Agulhus Current circulation from satellite remote sensing, *S. Afr. J. Sci.*, *77*(5), 231–236.

Manyilizu, M., F. Dufois, P. Penven, and C. J. C. Reason (2014), Interannual variability in the tropical western Indian Ocean, *Afr. J. Mar. Sci.*, 36(2), 233–252.

Mason, E., A. Pascual, and J. C. McWilliams (2014), A new sea surface height-based code for oceanic mesoscale eddy tracking, *J. Atmospheric Ocean. Technol.*, *31*(5), 1181–1188. doi: /10.1175/JTECH-D-14-00019.1.

Masumoto, Y., et al. (2004), A fifty-year eddy-resolving simulation of the world ocean: Preliminary outcomes of OFES (OGCM for the Earth Simulator), *J. Earth Simul.*, *1*, 35–56.

Masumoto, Y., and G. Meyers (1998), Forced Rossby waves in the southern tropical Indian Ocean, *J. Geophys. Res.*, *103*(C12), 27,589–27,602.

Matsuno, T. (1966), Quasi-geostrophic motions in the equatorial area, *J. Meteor. Soc. Japan*, *44*(1), 25–43.

Meyers, G. (1979), On the annual Rossby wave in the tropical North Pacific Ocean, *J. Phys. Oceanogr.*, *9*(4), 663–674.

Mo, K. C. (2000), Relationships between Low-Frequency Variability in the Southern Hemisphere and Sea Surface Temperature Anomalies, *J. Clim.*, *13*(20), 3599–3611.

Morioka, Y., K. Takaya, S. K. Behera, and Y. Masumoto (2015), Local SST impacts on the summertime mascarene high variability, *J. Clim.*, *28*(2), 678–694. doi:

/10.1175/JCLI-D-14-00133.1.

Nauw, J., H. Van Aken, A. Webb, J. R. E. Lutjeharms, and W. P. M. de Ruijter (2008), Observations of the southern East Madagascar Current and undercurrent and countercurrent system, *J. Geophys. Res.*, *113*(C8), doi:10.1029/2007JC004639.

Nonaka, M., Y. Sasai, H. Sasaki, B. Taguchi, and H. Nakamura (2016), How potentially predictable are midlatitude ocean currents? *Sci. Rep.*, *6*(1), 20153. doi: /10.1038/srep20153.

Ogawa, F., H. Nakamura, K. Nishii, T. Miyasaka, and A. Kuwano-Yoshida (2012), Dependence of the climatological axial latitudes of the tropospheric westerlies and storm tracks on the latitude of an extratropical oceanic front, *Geophys. Res. Lett.*, *39*(5), 1–5.

Ohishi, S., T. Tozuka, and M. F. Cronin (2017), Frontogenesis in the Agulhas Return Current Region Simulated by a High-Resolution CGCM, *J. Phys. Oceanogr.*, *47*(11), 2691–2710. doi: /10.1175/JPO-D-17-0038.1.

Palastanga, V., P. J. van Leeuwen, M. W. Schouten, and W. P. M. de Ruijter (2007), Flow structure and variability in the subtropical Indian Ocean: Instability of the South Indian Ocean countercurrent. *J. Geophys. Res.: Oceans*, *112*(1), 1–11. https://doi.org/10.1029/2005JC003395

Palastanga, V., P. J. van Leeuwen, and W. P. M. de Ruijter (2006), A link between low-frequency mesoscale eddy variability around Madagascar and the large-scale Indian Ocean variability, *J. Geophys. Res.*, 111, C09029, doi:10.1029/2005JC003081

Pedlosky, J., L. J. Pratt, M. A. Spall, and K. R. Helfrich (1997), Circulation around islands and ridges, *J. Mar. Res.*, *55*(6), 1199–1251.

Penven, P., J. R. E. Lutjeharms, and P. Florenchie (2006), Madagascar: A pacemaker for the Agulhas Current system? *Geophys. Res. Lett.*, *33*(17), 1–5. doi: /10.1029/2006GL026854.

Penven, P., V. Echevin, J. Pasapera, F. Colas, and J. Tam (2005), Average circulation, seasonal cycle, and mesoscale dynamics of the Peru Current System: A modeling approach, *J. Geophys. Res. Ocean*, *110*(10), 1–21. doi: /10.1029/2005JC002945.

Perigaud, C., and P. Delecluse (1993), Interannual sea level variations in the tropical Indian Ocean from Geosat and shallow water simulations, *J. Phys. Oceanogr.*, *23*(9), 1916–1934.

Pichevin, T., D. Nof, and J. R. E. Lutjeharms (1999), Why are there Agulhas rings?, *J. Phys. Oceanogr.*, 29(4), 693–707.

Ponsoni, L., B. Aguiar-González, H. Ridderinkhof, and L. R. M. Maas (2016), The East Madagascar Current: volume transport and variability based on long-term observations. *J. Phys. Oceanogr.*, 46(4), 1045-1065.

Pous, S., E. Feunteun, and C. Ellien (2010), Investigation of tropical eel spawning area in the South-Western Indian Ocean: Influence of the oceanic circulation, *Prog. Oceanogr.*, 86(3), 396–413, doi:10.1016/j.pocean.2010.06.002.

Putrasahan, D., B. P. Kirtman, and L. M. Beal (2016), Modulation of SST interannual variability in the Agulhas leakage region associated with ENSO, *J. Clim.*, *29*(19), 7089–7102, doi: /10.1175/JCLI-D-15-0172.1.

Qiu, B., and S. Chen (2010), Interannual-to-decadal variability in the bifurcation of the North Equatorial Current off the Philippines, *J. Phys. Oceanogr.*, *40*(11), 2525–2538.

Qiu, B., and S. Chen (2005). Variability of the Kuroshio Extension Jet, Recirculation Gyre, and Mesoscale Eddies on Decadal Time Scales, *J. Phys. Oceanogr., 35*(11), 2090–2103.

Qiu, B., and R. Lukas (1996), Seasonal and interannual variability of the North Equatorial Current, the Mindanao Current, and the Kuroshio along the Pacific western boundary, *J. Geophys. Res.*, *101*(C5), 12,315–12,330.

Randall, R. M., B. M. Randall, and D. Baird (1981), Speed of Movement of Jackass Penguins over Long Distances and their Possible Use of Ocean Currents. *S. Afr. J. Sci.*, *77*(9), 420–429.

Rao, S. A., and S. K. Behera (2005), Subsurface influence on SST in the tropical Indian Ocean: Structure and interannual variability, *Dyn. Atmos. Oceans*, *39*(1), 103–135.

Reason, C. J. C. (2001a), Subtropical Indian Ocean SST dipole events and southern African rainfall, *Geophys. Res. Lett.*, *28*(11), 2225–2227, doi: /10.1029/2000GL012735.

Reason, C. J. C. (2001b), Evidence for the influence of the Agulhas Current on regional atmospheric circulation patterns, *J. Clim.*, *14*(12), 2769–2778, doi: /10.1175/1520-0442(2001)014<2769:EFTIOT>2.0.CO;2.

Reason, C. J. C., and C. R. Godfred-Spenning (1998), SST variability in the South Indian Ocean and associated circulation and rainfall patterns over Southern Africa,

Meteor. Atmos. Phys., *66*(3), 243–258, doi: /10.1007/BF01026637.

Reason, C. J. C., C. R. Godfred-Spenning, R. J. Allan, and J. A. Lindesay (1998), Air–sea interaction mechanisms and low-frequency climate variability in the South Indian Ocean region, *Int. J. Climatol.*, *18*(4), 391–405, doi: /10.1002/(SICI)1097-0088(19980330)18:4<391::AID-JOC253>3.0.CO;2-C.

Ridderinkhof, W., D. Le Bars, A. Heydt, and W. Ruijter (2013), Dipoles of the South East Madagascar Current, *Geophys. Res. Lett.*, 40, 558–562, doi:10.1002/grl.50157

Rio, M.-H., S. Mulet, and N. Picot (2014), Beyond GOCE for the ocean circulation estimate: Synergetic use of altimetry, gravimetry, and in situ data provides new insight into geostrophic and Ekman currents, *Geophys. Res. Lett.*, 41, 8918–8925, doi:10.1002/2014GL061773.

Rouault, M., and P. Penven (2011), New perspectives on Natal Pulses from satellite observations, *J. Geophys. Res.*, 116, C07013, doi:10.1029/ 2010JC006866.

Rouault, M., S. A. White, C. J. C. Reason, J. R. E. Lutjeharms, and I. Jobard (2002), Ocean–Atmosphere Interaction in the Agulhas Current Region and a South African Extreme Weather Event, *Weather and Forecast.*, *17*(4), 655–669, doi: /10.1175/1520-0434(2002)017<0655:OAIITA>2.0.CO;2.

Rouault, M., and J. R. E. Lutjeharms (2000), Air-sea exchange over an Agulhas eddy at the subtropical convergence, *Global Atmos. Ocean Syst.*, *7*, 125–150.

Saji, N. H., B. N. Goswami, P. N. Vinayachandran, and T. Yamagata (1999), A dipole mode in the tropical Indian Ocean, *Nature*, 401(6751), 360–363.

Schouten, M. W., W. P. M. de Ruijter, and P. J. van Leeuwen (2002), Upstream control

of Agulhas Ring shedding, *J. Geophys. Res.*, 107(C8), doi:10.1029/2001JC000804.

Schouten, M. W., W. P. M. de Ruijter, P. J. van Leeuwen, and H. Ridderinkhof (2003), Eddies and variability in the Mozambique Channel, *Deep-Sea Res. Part II*, *50*(12–13), 1987–2003. doi: /10.1016/S0967-0645(03)00042-0.

van Sebille, E., C. N. Barron, A. Biastoch, P. J. van Leeuwen, F. C. Vossepoel, and W. P. M. de Ruijter (2009), Relating Agulhas leakage to the Agulhas Current retroflection location. *Ocean Sci.*, *5*(4), 511–521, doi: /10.5194/os-5-511-2009.

van Sebille, E., A. Biastoch, P. J. van Leeuwen, and W. P. M. de Ruijter (2009), A weaker Agulhas current leads to more Agulhas leakage, *Geophys. Res. Lett.*, *36*(3), 10–13, doi: /10.1029/2008GL036614.

Souza, J. M. A. C., C. de Boyer Montégut, and P. Y. Le Traon (2011), Comparison between three implementations of automatic identification algorithms for the quantification and characterization of mesoscale eddies in the South Atlantic Ocean, *Ocean Sci.*, *7*(3), 317–334, doi: /10.5194/os-7-317-2011.

Swallow, J., M. Fieux, and F. Schott (1988), The boundary currents east and north of Madagascar: 1. Geostrophic currents and transports, *J. Geophys. Res.*, 93(C5), 4951–4962.

Ting, M., Y. Kushnir, R. Seager, and C. Li (2009), Forced and internal twentieth-century SST trends in the North Atlantic, *J. Clim.*, *22*(6), 1469–1481, doi: /10.1175/2008JCLI2561.1.

Tozuka, T., T. Kataoka, and T. Yamagata (2014a), Locally and remotely forced atmospheric circulation anomalies of Ningaloo Niño/Niña, *Clim. Dyn.*, *43*(7–8),

2197–2205, doi: /10.1007/s00382-013-2044-x.

Tozuka, T., B. J. Abiodun, and F. A. Engelbrecht (2014b), Impacts of convection schemes on simulating tropical-temperate troughs over southern africa, *Clim. Dyn,*, *42*(1), 433– 451, doi:10.1007/s00382-013-1738-4.

Tozuka, T., T. Doi, T. Miyasaka, N. Keenlyside, and T. Yamagata (2011), Key factors in simulating the equatorial atlantic zonal sea surface temperature gradi- ent in a coupled general circulation model, *J. Geophys. Res.*, *116*, C06,010, doi: 10.1029/2010JC006717.

Tozuka, T., T. Miyasaka, A. Chakraborty, M. Mujumdar, S. Behera, Y. Masumoto, H. Nakamura, and T. Yamagata (2006), University of Tokyo coupled general circulation model (UTCM1.0)., *Ocean.-Atmos. Res. Rep.*, pp. 7–44.

Trenary, L. L., and W. Han (2012), Intraseasonal-to-interannual variability of South Indian Ocean sea level and thermocline: Remote versus local forcing, *J. Phys. Oceanogr.*, *42*(4), 602–627.

Tsugawa, M., and H. Hasumi (2010), Generation and Growth Mechanism of the Natal Pulse, *J. Phys. Oceanogr.*, *40*(7), 1597–1612, doi: /10.1175/2010JPO4347.1.

Uppala, S. M., et al. (2005), The ERA-40 re-analysis, *Quart. J. Roy. Meteorol. Soc.*, *131*(612), 2961–3012.

van der Werf, P. M., P. J. van Leeuwen, H. Ridderinkhof, and W. P. M. de Ruijter (2010), Comparison between observations and models of the Mozambique Channel transport: Seasonal cycle and eddy frequencies, *J. Geophys. Res.*, 115, C02002, doi:10.1029/2009JC005633.

Yamagata, T., S. K. Behera, J.-J. Luo, S. Masson, M. R. Jury, and S. A. Rao (2004), Coupled ocean-atmosphere variability in the tropical Indian Ocean, in *Earth's Climate*, edited by C. Wang, S. P. Xie, and J. A. Carton, pp. 189–211, American Geophysical Union.

Yuan, C., T. Tozuka, and T. Yamagata (2012), IOD influence on the early winter tibetan plateau snow cover: diagnostic analyses and an AGCM simulation, *Clim. Dyn.*, *39*(7), 1643–1660, doi:10.1007/s00382-011-1204-0.

Zhuang, W., M. Feng, Y. Du, A. Schiller, and D. Wang (2013), Low-frequency sea level variability in the southern Indian Ocean and its impacts on the oceanic meridional transports, *J. Geophys. Res.*, *118*(3), 1302–1315.